

Multiwavelength study of a young open cluster NGC 7419

Himali Joshi,^{1*} Brijesh Kumar,^{1,2} K. P. Singh,³ Ram Sagar,¹ Saurabh Sharma¹
and J. C. Pandey¹

¹*Aryabhata Research Institute of Observational Sciences, Manora Peak, Nainital 263 129, India*

²*Departamento de Física, Universidad de Concepción, Casilla 160-C, Concepción, Chile*

³*Tata Institute of Fundamental Research, Mumbai 400 005, India*

Accepted 2008 September 11. Received 2008 September 5; in original form 2007 October 14

ABSTRACT

Using new *UBVRIH α* CCD photometric observations and the archival infrared and X-ray data, we have carried out a multiwavelength study of a Perseus arm young open star cluster NGC 7419. An age of 22.5 ± 3.0 Myr and a distance of 3230^{+330}_{-430} pc are derived for the cluster. Our photometric data indicate a higher value of colour excess ratio $E(U - B)/E(B - V)$ than the normal one. There is an evidence for mass segregation in this dynamically relaxed cluster and in the range $1.4\text{--}8.6 M_{\odot}$, the mass function slope is in agreement with the Salpeter value. Excess emissions in near-infrared and $H\alpha$ support the existence of a young (≤ 2 Myr) stellar population of Herbig Ae/Be stars ($\geq 3.0 M_{\odot}$) indicating a second episode of star formation in the cluster region. Using *XMM-Newton* observations, we found several X-ray sources in the cluster region but none of the Herbig Ae/Be stars is detected in X-rays. We compare the distribution of upper limits for Herbig Ae/Be stars with the X-ray distribution functions of the T Tauri and the Herbig Ae/Be stars from previous studies, and found that the X-ray emission level of these Herbig Ae/Be stars is not more than $L_X \sim 5.2 \times 10^{30}$ erg s⁻¹, which is not significantly higher than for the T Tauri stars. Therefore, X-ray emission from Herbig Ae/Be stars could be the result of either unresolved companion stars or a process similar to T Tauri stars. We report an extended X-ray emission from the cluster region NGC 7419, with a total X-ray luminosity estimate of $\sim 1.8 \times 10^{31}$ erg s⁻¹ arcmin⁻². If the extended emission is due to unresolved emission from the point sources then we estimate ~ 288 T Tauri stars in the cluster region each having X-ray luminosity $\sim 1.0 \times 10^{30}$ erg s⁻¹. Investigation of dust attenuation and ¹²CO emission map of a square degree region around the cluster indicates the presence of a foreground dust cloud which is most likely associated with the local arm star-forming region (Sh2–154). This cloud harbours uniformly distributed pre-main-sequence stars ($0.1\text{--}2.0 M_{\odot}$), with no obvious trend of their distribution with either ($H - K$) excess or A_V . This suggests that the star formation in this cloud depend mostly upon the primordial fragmentation.

Key words: stars: emission-line, Be – stars: formation – stars: pre-main-sequence – X-rays: galaxies: clusters – X-rays: stars.

1 INTRODUCTION

NGC 7419 (R.A._{J2000} = 22^h54^m20^s, Dec._{J2000} = +60°48′54″; $l = 109^{\circ}.13$, $b = 1^{\circ}.12$) is a moderately populated young and heavily reddened open star cluster in Cepheus with a large number of Be stars. The cluster contains high-mass ($\geq 10 M_{\odot}$), intermediate-mass ($2\text{--}10 M_{\odot}$) and low-mass ($\leq 2 M_{\odot}$) stars. It is therefore an ideal laboratory for the study of initial stellar mass distribution as well as duration of star formation process in a molecular cloud. Presence of statistically significant number of Herbig Ae/Be stars in the cluster

makes it very attractive for understanding the formation of these stars and origin of various atmospheric activities like $H\alpha$ emission and X-ray emission in them. However, to address these questions in detail, one would like to know accurate distance and age parameters of the cluster NGC 7419, which is lacking despite a number of photometric and spectroscopic studies. This is mainly because of the fact that the cluster is heavily reddened in comparison to the nearby clusters situated at the similar distances, and suffers from variable reddening.

In order to determine cluster reddening reliably, accurate *UBV* broad-band photometry of early-type stars is essential. A comparison of the photometries available in the literature indicates that

*E-mail: himali@aries.ernet.in

UB data, many have systematic calibration error. For example, Beauchamp, Moffat & Drissen (1994) have mentioned that their colour may have an offset of ~ 0.2 mag due to the calibration problems in *U* band. Their photometric observations have been carried out in the poor seeing (2.5–4.0 arcsec) conditions. This will affect cluster photometric data particularly in the crowded regions.

The main goals of present study are to determine the distance, age and its spread and mass function (MF) of the cluster as accurate as possible. This will help us to understand the star formation history of the cluster, and to investigate the X-ray emission properties of Herbig Ae/Be stars. Deep optical *UBVRI* observations ($V \sim 22.0$ mag), narrow-band $H\alpha$ photometric observations along with the Two Micron All Sky Survey (2MASS), Infrared All Sky Survey (IRAS), Midcourse Space Experiment (MSX) and *XMM-Newton* archival data are used to understand the X-ray emission properties of Herbig Ae/Be stars, and the global scenario of star formation in the cluster NGC 7419 and its surrounding region.

Blanco et al. (1955) have reported the distance of this cluster as ~ 6 kpc based on the *RI* photometric observations. A similar value for cluster distance has also been obtained by Moffat & Vogt (1973). However, van de Hulst, Mullar & Oort (1954) have obtained a significantly smaller distance of 3.3 kpc. Using CCD data, a distance of 2.0 and 2.3 kpc was estimated by Bhatt et al. (1993) and Beauchamp et al. (1994), respectively. The age estimated by Bhatt et al. (1993) is ~ 40 Myr while Beauchamp et al. (1994) have estimated a much younger age of ~ 14 Myr. Recent CCD observations reported by Subramaniam et al. (2006) estimated its distance as 2.9 kpc and an age of 20–25 Myr.

The paper describes optical observations and the derivation of cluster parameters in Sections 2 and 3. The near-infrared (NIR) data are dealt in Section 4, while distribution of young stellar objects (YSOs), MF and mass segregation are given in Sections 5, 6 and 7. Finally, the X-ray data and its analysis (for the first time) are described in Section 8, followed by the summary and conclusions in Section 9.

2 PHOTOMETRIC DATA

2.1 Observations

The optical observations of NGC 7419 were carried out using a thinned back-illuminated CCD camera mounted at $f/13$ Cassegrain focus of the 104-cm Sampurnanand reflector telescope of Aryabhata Research Institute of Observational Sciences, Nainital. A $24 \mu\text{m}$ square size pixel of the 2048×2048 size CCD detector corresponds to 0.38 arcsec and the entire chip covers a field of about 13×13 arcmin² on the sky. In order to improve the signal-to-noise ratio, observations were taken in binned mode of 2×2 pixel. The gain and readout noise of the CCD are 10 electrons per analog-to-digital unit and 5.3 electrons, respectively. The journal of optical observations is given in Table 1. Broad-band Johnson *UBV*, Cousins *RI* and narrow-band $H\alpha$ line ($\lambda = 656.5$ nm) and $H\alpha$ continuum ($\lambda = 665$ nm) filters were used for observations. The narrow-band filters had a full width at half-maximum of 8 nm. Several bias and twilight flat-field frames in all the filters were taken to clean the images. Multiple long and short exposures were obtained for the cluster region. We observed 12 stars in Landolt (1992) standards field (SA98) covering a range in brightness ($11.93 < V < 15.90$) as well as in colour ($0.157 < (B - V) < 2.192$) for calibrating the cluster observations. The airmass range is covered from 1.1 to 2.0 for the Landolt (1992) standards, which was used for extinction determinations.

Table 1. Journal of CCD observations of the cluster NGC 7419 and the calibration region SA98 (Landolt 1992).

Date (UT)	Filter	Exposure time (s) (\times no. of exposures)
NGC 7419		
2005 October 30	$H\alpha$	$300 \times 2, 120 \times 2, 1500 \times 3$
	$H\alpha$ cont	$300 \times 2, 120 \times 2, 900 \times 3$
2005 November 7	<i>U</i>	$300 \times 3, 360 \times 4$
	<i>B</i>	$180 \times 4, 240 \times 4$
	<i>V</i>	$180 \times 4, 180 \times 4$
	<i>R</i>	$20 \times 4, 120 \times 4$
	<i>I</i>	$20 \times 4, 60 \times 4$
2005 November 8	<i>U</i>	1800×1
	<i>B</i>	1200×1
	<i>V</i>	900×1
	<i>R</i>	300×1
	<i>I</i>	500×1
2006 October 25	<i>U</i>	300×3
	<i>B</i>	300×2
	<i>V</i>	100×2
	<i>R</i>	20×2
	<i>I</i>	20×2
SA98		
2006 October 25	<i>U</i>	360×11
	<i>B</i>	150×10
	<i>V</i>	60×10
	<i>R</i>	25×10
	<i>I</i>	25×10

The photometric CCD data were reduced using the IRAF¹ and European Southern Observatory (ESO) MIDAS² data reduction packages. Photometry of the bias-subtracted and flat-fielded CCD frames was carried out using DAOPHOT-II software (Stetson 1987, 1992). Magnitude of the stars obtained from different frames was averaged separately for short and long exposures. When brighter stars were saturated on deep exposure frames, their magnitudes were taken only from unsaturated short exposure frames. We used DAOGROW program for construction of an aperture growth curve required for determining the difference between aperture and profile fitting magnitudes.

2.2 Calibrations

The instrumental magnitudes were converted into the standard system using least-square linear regression procedure outlined by Stetson (1992). The photometric calibration equations used are

$$u = U + (0.588 \pm 0.015)X + (-0.002 \pm 0.004)(U - B) + (6.933 \pm 0.006),$$

$$b = B + (0.347 \pm 0.013)X + (-0.035 \pm 0.005)(B - V) + (4.771 \pm 0.007),$$

$$v = V + (0.159 \pm 0.012)X + (-0.041 \pm 0.004)(V - I) + (4.320 \pm 0.007),$$

¹ IRAF – Image Reduction and Analysis Facility is distributed by the National Optical Astronomy Observatories, which are operated by the Association of Universities for Research in Astronomy, Inc., under cooperative agreement with the National Science Foundation (<http://iraf.noao.edu>).

² MIDAS – Munich Image Data Analysis System is developed and maintained by ESO.

Table 2. The mean photometric errors (σ) in magnitude are given as a function of brightness range in the cluster region.

Magnitude range	σ_U	σ_B	σ_V	σ_R	σ_I
<14	0.009	0.002	0.003	0.005	0.007
14–15	0.007	0.005	0.003	0.005	0.004
15–16	0.021	0.010	0.013	0.012	0.025
16–17	0.030	0.015	0.010	0.011	0.023
17–18	0.069	0.018	0.010	0.012	0.026
18–19	0.131	0.029	0.014	0.011	0.031
19–20		0.070	0.017	0.013	0.026
20–21		0.173	0.031	0.019	0.031
21–22			0.082	0.036	0.034
22–23			0.196	0.061	0.047

$$r = R + (0.139 \pm 0.009)X + (-0.056 \pm 0.007)(V - R) + (4.234 \pm 0.006),$$

$$i = I + (0.104 \pm 0.007)X + (-0.048 \pm 0.003)(V - I) + (4.767 \pm 0.005),$$

where U , B , V , R and I are the standard magnitudes; u , b , v , r and i are the instrumental magnitudes obtained after time and aperture correction and X is the airmass. We have ignored the second-order colour correction terms as they are generally small in comparison to the internal photometric errors as given by DAOPHOT. The photometric errors as a function of brightness range are given in Table 2. It can be seen that the errors become large (≥ 0.1 mag) for stars fainter than $V \approx 22$ mag, and hence the measurements beyond this magnitude are less reliable and are not considered in further analysis. At V band, we could detect 1817 stars in 13×13 arcmin² region and their photometric magnitudes are given in Table 3 (full table available only in electronic form). The difference of calibrated magnitudes derived using above transformation to that of the Landolt (1992) magnitudes are plotted in Fig. 1. We generated secondary standards in the cluster field using data of 2006 October 25 to standardize the data observed on 2005 November 7 and 8. We, therefore, also plot differences in magnitudes of the secondary standards on these dates. No systematic effect has been seen in the residuals from night-to-night and its distribution is random in nature with a typical accuracy of ~ 0.03 mag in $UBVRI$ band.

Fig. 2 shows a comparison of the present CCD photometry with the previously reported CCD photometry by Bhatt et al. (1993), Beauchamp et al. (1994) and Subramaniam et al. (2006). The difference Δ (present – literature) is plotted as a function of V magnitude and a detailed statistics are given in Table 4 (full table available only in electronic form). In comparison to the photometric data of Beauchamp et al. (1994), the $(B - V)$ colours obtained by us are bluer by ~ 0.25 mag, $(U - B)$ colours are redder by ~ 0.25 mag and the V magnitude is fainter by ~ 0.05 mag. Our photometry is in

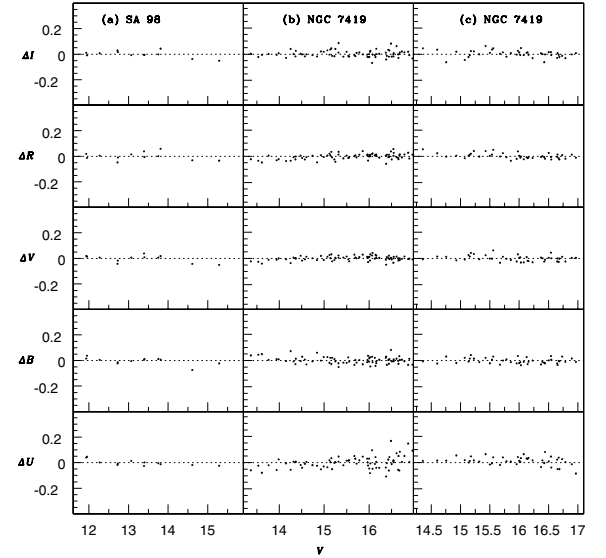


Figure 1. Difference in $UBVRI$ magnitude measurements as a function of V magnitude are shown. The left-hand panels (a) show the residuals of standard magnitude from Landolt (1992) and the present transformed magnitudes, while the middle panels (b) and right-hand panels (c) show magnitude difference of secondary standards as generated on 2006 October 25 to that of on 2005 November 7 and 8, respectively.

agreement with Bhatt et al. (1993) and Subramaniam et al. (2006). It is worth pointing out that our data is ~ 2.0 mag deeper from Bhatt et al. (1993) and Subramaniam et al. (2006), i.e. $V \sim 22.0$ mag.

2.3 Completeness of the data

The completeness of the data used in the present work was estimated using the ADDBSTAR routine of the DAOPHOT-II. In brief, the method consists of randomly adding artificial stars (about 10–15 per cent of the originally detected stars) of known magnitudes and positions into the original frames. The frames were rereduced using the same procedure used for the original frames. The ratio of the number of recovered stars to those added in each magnitude interval gives the completeness factor (CF) as a function of magnitude. The CF was obtained using the stars which were recovered in both V and I passbands. The detailed procedures have been outlined elsewhere (Sagar & Richtler 1991; Sagar & Griffiths 1998; Pandey et al. 2001; Nilakshi & Sagar 2002). The CF as a function of V magnitude is given in Table 5.

2.4 $H\alpha$ photometric data

To identify emission-line stars, we use α index ($m_{6565} - m_{6650}$) parameter, where m_{6565} and m_{6650} are the magnitude of a star in the $H\alpha$ and

Table 3. $UBVRI$ and $H\alpha$ photometric data of the sample stars in 13×13 arcmin² region. X and Y positions of stars in the CCD are converted into R.A._{J2000} and Dec._{J2000} using the Guide Star Catalogue II (GSC 2.2, 2001). The full table is available online. Please see the Supporting Information section for details.

ID	R.A. _{J2000} (h m s)	Dec. _{J2000} (° ′ ″)	X (pixel)	Y (pixel)	U (mag)	B (mag)	V (mag)	R (mag)	I (mag)	$H\alpha$ index (mag)
1	22 54 06.38	+60 52 13.30	818.710	640.714	12.999 ± 0.002	12.481 ± 0.002	11.707 ± 0.009	11.321 ± 0.012	11.003 ± 0.002	0.032 ± 0.008
2	22 54 02.22	+60 54 57.20	1032.410	691.088	13.518 ± 0.002	12.964 ± 0.002	12.156 ± 0.009	11.761 ± 0.011	11.381 ± 0.004	0.038 ± 0.006
3	22 53 30.17	+60 53 38.60	914.148	994.003	13.964 ± 0.003	13.492 ± 0.002	12.740 ± 0.002	12.321 ± 0.010	11.946 ± 0.004	0.022 ± 0.020
–	–	–	–	–	–	–	–	–	–	–

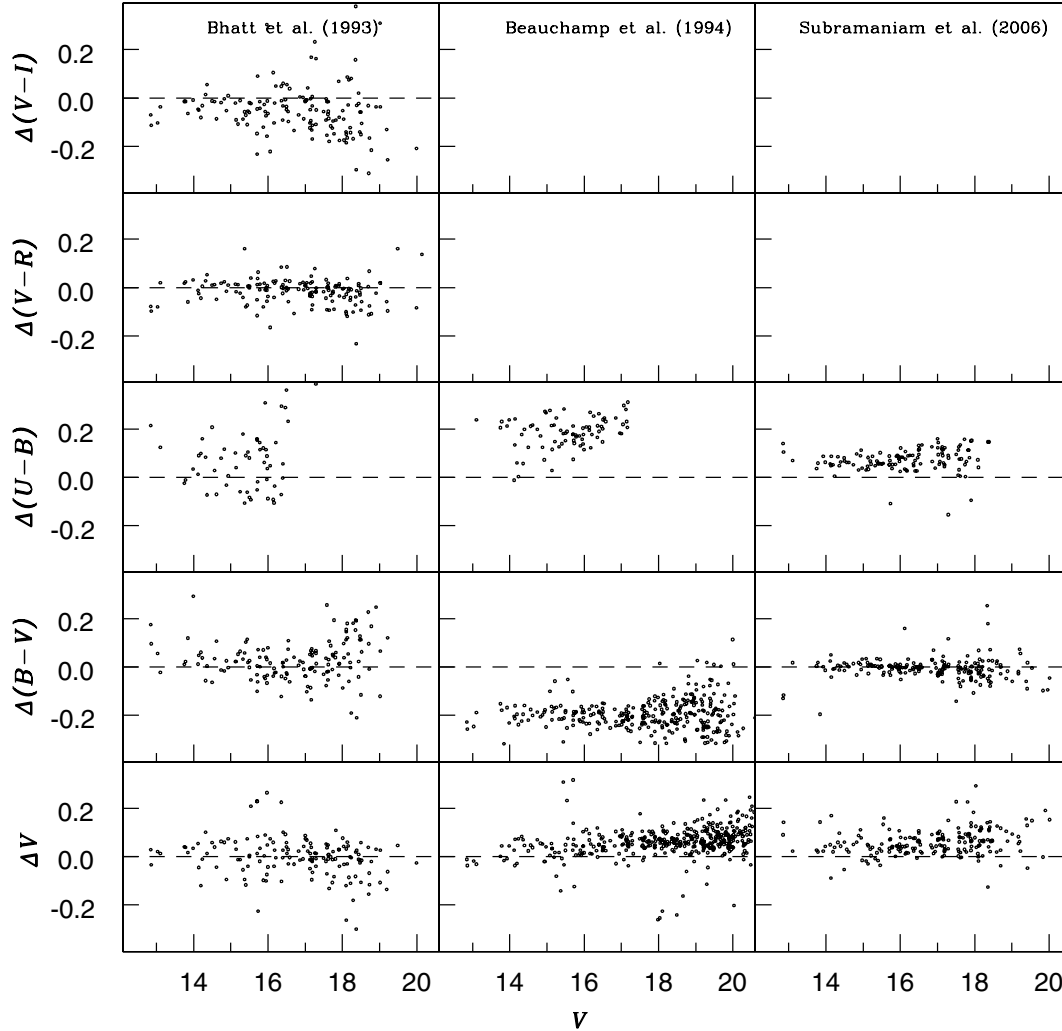


Figure 2. Comparison of present CCD photometry with that available in the literature. The difference Δ (present – literature) is in magnitude. The dashed line drawn in each panel represents zero difference.

Table 4. A comparison of present *UBVRI* CCD photometry with that present in the literature – viz Bhatt et al. (1993), Beauchamp et al. (1994) and Subramaniam et al. (2006). The full table is available online. Please see the Supporting Information section for details.

<i>V</i> range	$\langle \Delta V \rangle$ Mean $\pm \sigma$	$\langle \Delta(B - V) \rangle$ Mean $\pm \sigma$	$\langle \Delta(U - B) \rangle$ Mean $\pm \sigma$	$\langle \Delta(V - R) \rangle$ Mean $\pm \sigma$	$\langle \Delta(V - I) \rangle$ Mean $\pm \sigma$
Bhatt et al. (1993)					
<14.0	0.025 \pm 0.030 (8)	0.060 \pm 0.070 (6)	0.030 \pm 0.083 (4)	-0.022 \pm 0.065 (7)	-0.044 \pm 0.034 (6)
-	-	-	-	-	-

$H\alpha$ -continuum filter, respectively. In an area of 13×13 arcmin², we could measure α index for 1065 stars and the same is plotted against $(R - I)$ colours in Fig. 3. We estimated a mean α index iteratively for these stars by 3σ clipping. Seven such iterations resulted in a constant mean value of 0.097 mag and an rms scatter (σ) of 0.116 mag. Stars having α index within 3σ are therefore considered as having normal strength at $H\alpha$ feature. A star is considered as $H\alpha$ emitter if $\alpha \leq -0.25$ mag and $H\alpha$ absorber if $\alpha \geq 0.44$ mag. The observed characteristics of stars with $H\alpha$ emission are given in Table 6. $H\alpha$ emission stars reported only by others in the literature

are also listed in Table 6. This could be due to the variable nature of $H\alpha$ emission from the stars.

We detect 29 $H\alpha$ emission-line stars, and along with 15 more reported by Pigulski & Kopacki (2000) and Subramaniam et al. (2006), the total number of $H\alpha$ emission-line stars in the 13×13 arcmin² region around the cluster have now increased to 44. Of these, 13 are newly identified in the present work. Though some late-type dwarfs do show strong chromospheric $H\alpha$ in emission, but a few false detection may not be ruled out. As a non-emission late-type star generally has a series of strong metal oxide absorption lines,

Table 5. CF of the photometric data as a function of brightness and location.

Magnitude range (V mag)	NGC 7419		Field region
	$r \leq 1$ arcmin	$1 \leq r \leq 3.5$ arcmin	$3.5 \leq r \leq 5$ arcmin
13–14	1.00	1.00	1.00
14–15	1.00	1.00	1.00
15–16	1.00	1.00	1.00
16–17	1.00	0.98	0.99
17–18	0.89	0.97	0.98
18–19	0.57	0.93	0.96
19–20	0.59	0.89	0.97
20–21	0.60	0.86	0.93
21–22	0.15	0.38	0.47

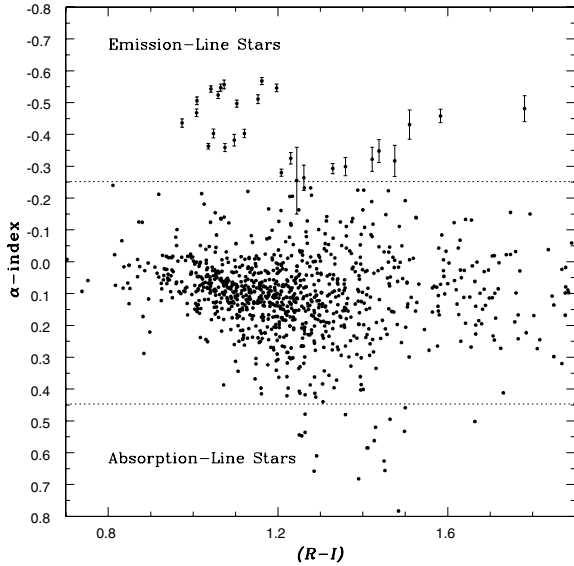


Figure 3. The α index as a function of colour ($R - I$). The dashed line represents the 3σ limits from a mean α index of 0.096 ± 0.116 mag. Emission-line stars having α index ≤ -0.252 mag are shown with error bars. The absorption-line stars denote α index ≥ 0.444 mag.

such as TiO in its spectrum and this may lead to an underestimation of their continuum, hence making the star an $H\alpha$ emitter (e.g. Huang, Chen & Hsiao 2006).

3 PROPERTIES OF THE CLUSTER

3.1 Radial density profile

We estimate the cluster centre iteratively by calculating average X and Y positions of stars with $V \leq 18.0$ mag within 80 pixel from eye estimated centre, until it converged to a constant value. The coordinates of the cluster centre are found to be $R.A._{J2000} = 22^{\text{h}}54^{\text{m}}18^{\text{s}}$ and $Dec._{J2000} = +60^{\circ}48'58''$. Using this method, a typical error expected in locating the centre is 5 arcsec. To estimate extent of the cluster, we divide the cluster region into a number of concentric circles with an annulus of width 30.5 arcsec. The projected radial stellar density profile is plotted in Fig. 4 for three magnitude limits – e.g. $V = 17, 18, 20$ mag. The error bars denote Poisson statistics.

The $\rho(r)$ is parametrized as (King 1962; Kaluzny & Udalski 1992)

$$\rho(r) \propto \frac{f_0}{1 + (r/r_c)^2}, \quad (1)$$

where r_c and f_0 are the core radius of the cluster and central star density, respectively. As the observed area (13×13 arcmin²) is large compared to the cluster diameter, we estimate f_b using outer region ($r > 5$ arcmin) of the cluster and to derive f_0 and r_c , we performed a Levenberg–Marquardt non-linear fitting routine (Press et al. 1992) to equation (1). The fitted parameters are shown in Fig. 4. We define extent of the cluster (r_{cl}) as the radius at which $\rho(r)$ equals 3σ level above the field star density. Using optical data, we have estimated the core radius of about 1 arcmin and cluster radius of 4.0 ± 0.5 arcmin for the cluster. This is also supported by the radial density profile fits at 2MASS K -band data. The catalogue of open cluster by Dias et al. (2002) have been reported the radius of the cluster as 2.5 arcmin. To reduce the effect of field star contamination, we, therefore, consider lower limit of radius as 3.5 arcmin for further analysis.

3.2 Colour–magnitude diagrams

The V , $(U - B)$; V , $(B - V)$ and V , $(V - I)$ colour–magnitude diagrams (CMDs) of the cluster region along with V , $(V - I)$ CMD of the field region are shown in Fig. 5. Morphology of the CMDs is typical of a young-age open star cluster and the main sequence extends down to $V \sim 22.0$ mag in V , $(V - I)$ CMD. It is seen that the field star contamination becomes more evident for stars with $V > 18$ mag, therefore, a statistical criteria was used to remove the field star contamination, following procedure adopted by Sandhu, Pandey & Sagar (2003). For this purpose, we assume a uniform distribution of field stars in an area outside the cluster region ($r > 3.5$ arcmin). The luminosity function (LF) derived from the V , $(V - I)$ CMD of the field region was subtracted from the LF of the cluster region. For a randomly selected star in the V , $(V - I)$ CMD of field region, the nearest star in the V , $(V - I)$ CMD of cluster region within $V \pm 0.25$ mag and $(V - I) \pm 0.125$ mag of the field star was removed. The necessary corrections for CF have also been considered in statistical subtraction. Statistical subtraction of data have been done till $V \approx 21.0$ mag only as they have CF value > 0.5 . The V , $(V - I)$ diagram of statistically cleaned cluster sample is shown in Fig. 5. Further, to select main-sequence members more reliably, we define blue and red envelope in statistically cleaned CMD and the same is shown in the left-hand panel of Fig. 6.

3.3 Interstellar reddening

3.3.1 Law of interstellar reddening

We investigated the nature of interstellar reddening towards the cluster direction using the colour excess ratio method as described by Johnson (1968). We select stars with spectral types earlier than A0 by applying criterion of $V < 17.7$ and $1.35 < (B - V) < 1.70$ on probable members of the cluster (Section 3.2). From this list we exclude stars showing either $H\alpha$ emission (see Section 2.4) or NIR excess (see Section 4) as their reddening properties are likely to be different from the normal stars (Kumar et al. 2004). We estimate intrinsic colours using Q method (cf. Johnson & Morgan 1953) and iteratively estimate reddening free parameter Q [$= (U - B) - X(B - V)$, where $X = E(U - B)/E(B - V)$], till the colour excess ratios become constant within the photometric errors. For the first iteration, we assume $X = 0.72$. The colour excesses are determined using intrinsic colours as derived from the MKK spectral type–luminosity class colour relation given by Caldwell et al. (1993) for

Table 6. Photometric properties of 44 H α emission-line stars in 13×13 arcmin² region around NGC 7419 are tabulated. Columns (1)–(9) are taken from the present work. Column (10) carry comments on the stars identified in the present and previous work – ‘Yes’ stands for detection and ‘No’ for non-detection in the present work, ‘BMD’ for Beauchamp et al. (1994), ‘PK’ for Pigulski & Kopacki (2000), ‘Sub’ for Subramaniam et al. (2006) along with their identification in braces. Stars located outside the cluster region (see Section 2.4) are indicated with ‘field’.

ID	R.A. _{J2000} (h m s)	Dec. _{J2000} (° ′ ″)	<i>X</i> (pixel)	<i>Y</i> (pixel)	<i>V</i> (mag)	<i>R</i> (mag)	α index (mag)	<i>R</i> – <i>I</i> (mag)	Remark (10)
(1)	(2)	(3)	(4)	(5)	(6)	(7)	(8)	(9)	(10)
12	22 54 14	60 48 39	541.2	549.5	13.75	12.63	–0.36	+1.08	Yes, BMD(389), PK, Sub(M)
15	22 54 39	60 47 24	454.5	310.5	13.93	12.96	–0.01	+0.97	No, BMD(1129), PK
18	22 54 26	60 49 02	576.0	442.9	14.12	13.15	–0.10	+0.96	No, BMD(781), PK, Sub(C)
19	22 54 20	60 49 52	639.5	496.0	14.14	13.05	–0.40	+1.05	Yes, BMD(620), PK, Sub(G)
20	22 54 15	60 49 50	634.7	545.2	14.14	13.11	–0.18	+1.03	No, BMD(417), PK, Sub(J)
21	22 54 23	60 50 04	656.1	473.7	14.20	13.07	–0.38	+1.10	Yes, BMD(702), PK, Sub(4)
23	22 54 23	60 49 53	642.3	475.6	14.23	13.09	–0.56	+1.07	Yes, BMD(692), PK, Sub(3)
27	22 54 20	60 48 36	539.0	499.1	14.36	13.33	–0.21	+1.02	No, BMD(585), PK, Sub(I)
29	22 54 37	60 48 36	547.6	335.7	14.39	13.23	–0.50	+1.10	Yes, BMD(1076), PK, Sub(A)
38	22 54 27	60 48 52	564.0	428.1	14.88	13.76	–0.54	+1.04	Yes, BMD(831), PK, Sub(B)
39	22 54 20	60 48 54	563.3	492.1	14.93	13.92	–0.05	+1.04	No, BMD(621), PK, Sub(K)
48	22 54 18	60 48 57	566.2	517.2	15.14	14.08	–0.50	+1.01	Yes, BMD(504), PK, Sub(L)
57	22 54 26	60 49 05	581.2	435.0	15.37	14.30	–0.24	+0.81	No, BMD(815), PK, Sub(2)
59	22 54 08	60 50 23	673.6	621.9	15.44	14.18	–0.55	+1.20	Yes, BMD(239), PK, Sub(5)
64	22 54 16	60 47 49	476.0	532.4	15.54	14.32	–0.57	+1.16	Yes, BMD(427), PK, Sub(N)
66	22 54 14	60 46 20	358.0	543.2	15.56	14.51	–0.22	+1.13	No, BMD(375), Sub(P)
69	22 54 24	60 49 31	613.6	463.4	15.70	14.69	–0.44	+0.97	Yes, BMD(728), PK, Sub(D)
71	22 54 20	60 48 51	559.3	500.3	15.71	14.76	–0.08	+0.96	No, BMD(582), PK, Sub(H)
73	22 54 32	60 47 57	494.2	374.4	15.72	14.65	+0.04	+1.15	No, BMD(967), PK
74	22 54 10	60 49 39	617.3	595.2	15.73	14.67	+0.06	+0.59	No, BMD(290), PK
75	22 54 29	60 49 08	586.1	408.3	15.78	14.68	–0.52	+1.06	Yes, BMD(884), PK, Sub(1)
81	22 54 17	60 48 23	520.3	526.5	15.95	14.98	–0.02	+0.99	No, BMD(451), PK
85	22 54 17	60 48 18	514.4	524.8	15.97	14.93	+0.05	+1.06	No, BMD(458), PK
89	22 54 15	60 51 22	755.0	556.0	16.01	14.92	–0.55	+1.06	Yes, Sub(Q)
91	22 54 13	60 50 09	658.0	572.1	16.06	15.00	–0.01	+1.13	No, BMD(351), PK
95	22 54 17	60 51 37	776.5	535.6	16.11	15.10	–0.47	+1.01	Yes, Sub(R)
110	22 54 26	60 47 57	491.7	435.1	16.35	15.28	–0.36	+1.04	Yes, BMD(795), PK, Sub(6),
126	22 54 12	60 48 33	532.6	569.7	16.50	15.43	–0.01	+1.13	No, BMD(340), PK
127	22 54 19	60 48 14	509.7	506.9	16.50	15.45	–0.08	+1.11	No, BMD(551), PK
139	22 54 24	60 47 36	462.8	450.1	16.65	15.43	–0.51	+1.15	Yes, BMD(745), Sub(E)
145	22 54 07	60 48 17	508.8	618.9	16.71	15.33	–0.29	+1.33	Yes
181	22 54 51	60 48 27	543.4	199.9	17.07	15.95	–0.28	+1.21	Yes, field
218	22 54 24	60 47 01	416.6	447.5	17.32	16.17	–0.40	+1.12	Yes, BMD(741), PK, Sub(F)
321	22 54 13	60 50 27	681.9	572.7	18.13	16.92	–0.32	+1.23	Yes, BMD(352),
438	22 54 38	60 52 10	829.5	331.6	18.81	17.55	–0.30	+1.36	Yes, field
– ^a	22 53 33	60 45 51	300.2	938.4	18.87	17.27	–0.28	+2.11	Yes, field
655	22 54 56	60 47 41	485.2	148.1	19.53	18.14	–0.46	+1.58	Yes, field
703	22 53 37	60 53 22	895.1	925.5	19.65	18.45	–0.26	+1.24	Yes, field
714	22 54 40	60 49 24	612.6	306.4	19.68	18.40	–0.35	+1.44	Yes, BMD(1157)
716	22 54 57	60 53 38	954.5	157.8	19.68	18.37	–0.32	+1.42	Yes, field
791	22 55 05	60 53 02	911.0	82.3	19.90	18.52	–0.43	+1.51	Yes, field
801	22 54 34	60 51 19	760.3	366.9	19.92	18.59	–0.32	+1.47	Yes
808	22 54 40	60 48 31	542.9	303.1	19.94	18.70	–0.26	+1.26	Yes, BMD(1153)
831	22 54 13	60 45 59	329.3	553.2	20.01	18.45	–0.48	+1.78	Yes

^aError in *V* magnitude is greater than 0.1 mag.

(*U* – *B*), (*B* – *V*), (*V* – *R*) and (*V* – *I*) and by Koornneef (1983) for (*V* – *J*), (*V* – *H*) and (*V* – *K*). Mean values of colour excess ratios derived for the cluster are given in Table 7 and except *X*, all other colour excess ratios are in agreement with that expected for normal interstellar matter (Cardelli, Clayton & Mathis 1989). The value of *X* ($\sim 0.90 \pm 0.08$) is significantly greater than the normal value of ~ 0.72 , which implies that the average dust grain sizes are smaller than average. The ratio of total-to-selective extinction is estimated using the relation $R_V = 1.1E(V - K)/E(B - V)$ (Whittet & van Breda 1980) and it is found to be 3.2 ± 0.1 .

We have also determined the value of colour excess ratios using our *UBVRI* photometry and spectral classification of six stars (see Table 8) available in the literature (Beauchamp et al. 1994; Caron et al. 2003). Intrinsic colours³ are read from Wegner (1994) for (*V* – *R*) and (*V* – *I*), from Fitzgerald (1970) for (*U* – *B*). The mean value of *X* ($=0.88 \pm 0.06$) using this method is in good agreement with the one derived from iterative *Q* method. Further, the excess

³The intrinsic colours of Johnson *RI* in Wegner (1994) are converted into Cousins *RI* using Bessell (1979) transformation relations.

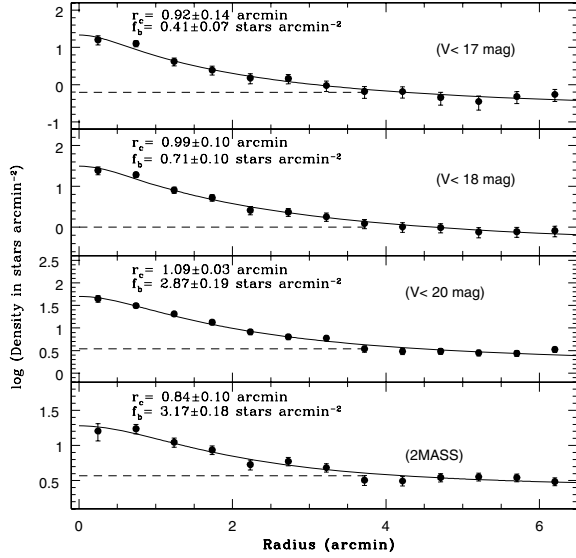


Figure 4. Projected radial stellar density profile of NGC 7419. Dashed lines represent 3σ levels above the field star density and solid curve shows best fit to the empirical model of King (1962).

ratios at other wavebands, and mean value of $R_V (= 3.16 \pm 0.10)$ are also close to the one derived using Q method (see Table 8).

Higher value of colour excess ratio X , as found above, is also supported by the V , $(U - B)$ CMD (Fig. 5), in which the isochrones (Girardi et al. 2002, hereafter GRD02) are found to fit well with $X = 0.90$. Such anomalous values of X are not uncommon for the interstellar matter in the Milky Way and a higher value of X (> 0.72) has also been reported along lines of sight of other star-forming clusters, for example, NGC 869 ($X = 0.90$; Pandey et al. 2003); Markarian 50 ($X = 0.81$; Baume, Vázquez & Carraro 2004) and NGC 7510 ($X = 0.78$; Barbon & Hassan 1996). However, they report normal value for other colour excesses in these clusters. For further analysis, we have therefore used the normal value of colour excess ratios except for the value $E(U - B)/E(B - V)$, which is adopted as 0.90.

3.3.2 Determination of reddening

Fig. 7 shows observed colour–colour, $(U - B)$, $(B - V)$, diagram for the cluster region. To determine reddening $E(B - V)$, the intrinsic

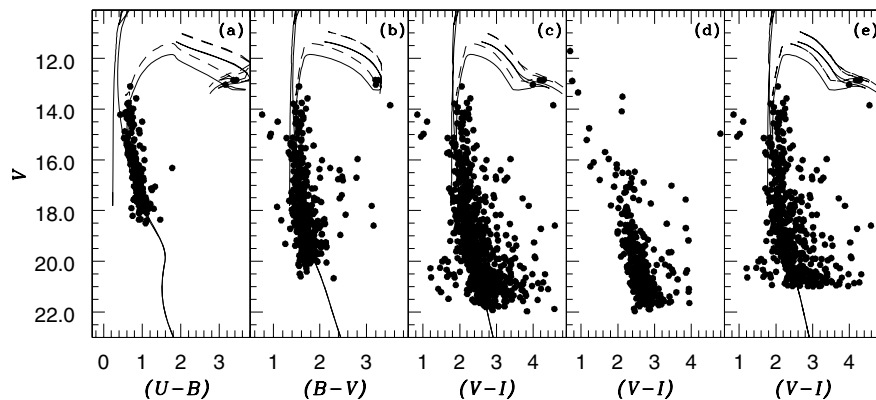


Figure 5. CMDs for cluster regions are shown in panels (a) V , $(U - B)$, (b) V , $(B - V)$ and (c) V , $(V - I)$. Panel (d) is for field region and the statistically cleaned V , $(V - I)$ CMD for cluster is shown in panel (e). Theoretical isochrones from GRD02 are shown with continuous lines for $\log(\text{age}) = 6.6, 7.3$ and 7.4 Myr in the panels (a), (b), (c) and (e).

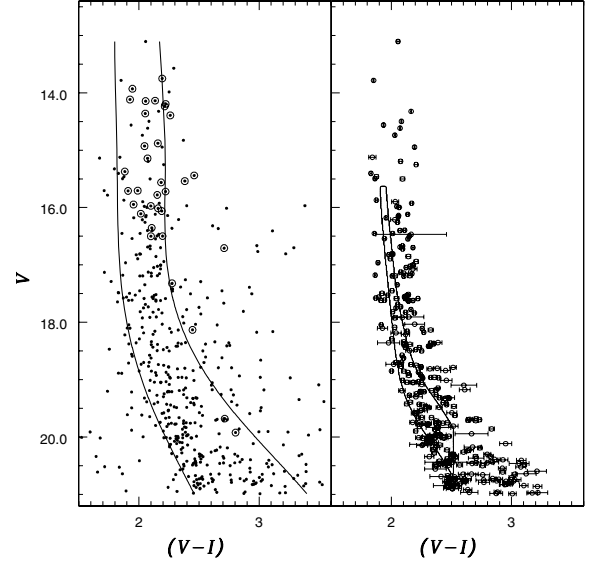


Figure 6. Statistically cleaned V , $(V - I)$ CMD for NGC 7419. Left-hand panel: solid lines confine the blueward and redward boundary of the main sequence. Emission-line stars are encircled. Right-hand panel: solid curves show the best-fitting Padova isochrone obtained using τ^2 minimization method (Naylor & Jeffries 2006) for fixed $z = 0.019$ and age = 25 Myr with distance as free parameter. Horizontal bars denote errors in $(V - I)$. See Section 3.5 for further details.

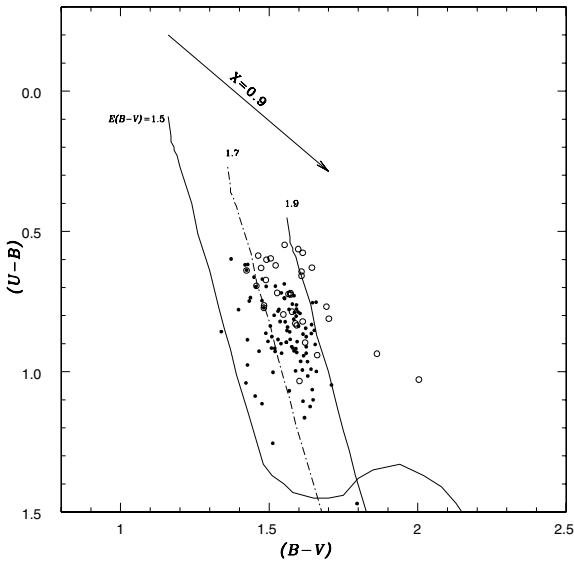
colours for main-sequence stars with solar metallicity (Schmidt-Kaler 1982) are reddened along the reddening vector ($X = 0.9$). This reddened main sequence suggests that $E(B - V)$ for the cluster region varies from 1.5 to 1.9 mag, with a visual mean value of about 1.7 mag. This reddening variation (~ 0.4 mag) for cluster members is well above the typical width of intrinsic main-sequence stars, i.e. ≤ 0.11 mag, which is caused usually due to photometric accuracy and the presence of binary stars (Sagar et al. 1987). It therefore indicates the presence of variable reddening within the cluster region, which is also reported by Subramaniam et al. (2006). Few emission-line stars (open circles) are found to have $E(B - V) > 1.9$ mag and these may either be embedded deep in the parent cloud or be surrounded with circumstellar matter. Using iterative Q method (Section 3.3.1), we derive mean value of $E(B - V)$ as 1.7 ± 0.2 mag, which is same as estimated visually by colour–colour diagram, and hence we adopt this value in our further analysis.

Table 7. Observed colour excess ratios in the direction of NGC 7419 are listed along with the excess ratios valid for normal interstellar reddening law, $R_V = 3.1$ (Cardelli et al. 1989).

Object	$\frac{E(U-B)}{E(B-V)}$	$\frac{E(V-R)}{E(B-V)}$	$\frac{E(V-I)}{E(B-V)}$	$\frac{E(U-B)}{E(V-J)}$	$\frac{E(B-V)}{E(V-J)}$	$\frac{E(V-R)}{E(V-J)}$	$\frac{E(V-I)}{E(V-J)}$	$\frac{E(V-H)}{E(V-J)}$	$\frac{E(V-K)}{E(V-J)}$
NGC 7419	0.90 ± 0.09	0.62 ± 0.02	1.29 ± 0.04	0.37 ± 0.04	0.41 ± 0.01	0.25 ± 0.01	0.52 ± 0.01	1.14 ± 0.01	1.20 ± 0.02
Normal value	0.72	0.62	1.25	0.32	0.43	0.27	0.56	1.13	1.21

Table 8. Giant stars with known spectral types in the literature (Beauchamp et al. 1994; Caron et al. 2003). Colour excess ratios are derived using present data.

ID	BMD ID	Spectral type	$E(B-V)$	$\frac{E(U-B)}{E(B-V)}$	$\frac{E(V-R)}{E(B-V)}$	$\frac{E(V-I)}{E(B-V)}$	$\frac{E(V-K)}{E(B-V)}$	$R_V = 1.1 \frac{E(V-K)}{E(B-V)}$
8	687	B2.5 II	1.741	0.883	0.641	1.283	2.924	3.216
13	473	B2.5 III	1.648	0.891	0.623	1.245	2.754	3.030
15	1129	B4.0 III	1.669	0.752	0.639	1.266	2.833	3.116
16	190	B0.0 III	1.999	0.924	0.642	1.267	2.837	3.120
20	417	B1/2 III	1.845	0.912	0.638	1.263	2.903	3.193
12	389	B1/2 III	1.789	0.896	0.670	1.313	3.014	3.315

**Figure 7.** The $(B-V)$, $(U-B)$ colour-colour diagram for stars in the cluster region. Open circles represent stars with $H\alpha$ emission. Solid lines are intrinsic main sequence reddened along the reddening line with $E(B-V) = 1.5$ and 1.9 mag, while the dotted line is for 1.7 mag.

3.4 Turn-off age of the cluster

Turn-off age of the cluster is determined by comparing the theoretical stellar evolutionary models, the Padova isochrones (GRD02) for solar metallicity $Z = 0.019$ with observed CMDs (see Fig. 5). Theoretical isochrones for ages 4, 20 and 25 Myr, corrected for the mean reddening $E(B-V) = 1.7$ mag, are shown with solid lines and are visually fitted to the bluest envelope of CMDs consisting of probable members as selected in Section 3.2. It is found that $X = 0.9$ results in a better isochrone fit in V , $(U-B)$ CMD than the normal value, $X = 0.72$ (Section 3.3.1). Locations of the red supergiants (Caron et al. 2003) BMD 921 (M2.5 Iab), BMD 696 (M2.5 Iab) and BMD 435 (M2.5 Iab) are found to be consistent with the isochrones, while BMD 139 (M3.5I) and BMD 950 (M7.5), both pulsating supergiants were prone to produce more scatter in distance and age estimate of NGC 7419. Thus, using the visual-fit method, the present

data find the turn-off age of the cluster to lie between 19 and 25 Myr and hence we assign an age of 22.5 ± 2.5 Myr.

We also estimate age using morphological age method (Phelps, Janes & Montgomery 1994; Pandey et al. 1997), which employs colour-index parameter (CIP), defined as the difference in the colour index between the blue turnoff point of the main sequence and the colour at the base of the red giant branch. For NGC 7419, CIP is calculated as 1.654 mag and it represents the age between 20 and 25 Myr, which is in good agreement with our previous value. The present age estimate is similar to the one derived by Subramaniam et al. (2006) less than the 50 Myr given by Bhatt et al. (1993) and older than 14 Myr derived by Beauchamp et al. (1994).

3.5 Distance to the cluster

The zero-age main-sequence fitting procedure (Fig. 5) is used to derive the distance of the cluster and the distance modulus is estimated as 12.45 ± 0.20 mag which corresponds to a distance of 3100 ± 290 pc. The distance determination is further performed using a maximum likelihood τ^2 -minimization method which employs fitting two-dimensional distributions to stellar data in colour-magnitude space (Naylor & Jeffries 2006; Jeffries et al. 2007; Mayne et al. 2007). This takes into account the effects of binary population as well as observed photometric errors. Assuming an age of ~ 22.5 Myr and a binary fraction of 0.5, the best-fitting Padova isochrone with solar metallicity yields a distance modulus of 12.55 mag (Fig. 6, Section 3.2). Emission-line stars were excluded from this fit. Adding a systematic error of 0.28 mag due to differential reddening to each data point would result $P_r(\tau^2) = 0.5$ with 68 per cent confidence ranges from 12.24 to 12.76 mag. We, therefore, adopt a distance of 3230^{+330}_{-430} pc for NGC 7419, which is similar to the estimate of Subramaniam et al. (2006) but higher from the value reported by Bhatt et al. (1993) and Beauchamp et al. (1994).

4 NEAR-INFRARED DATA AND INTERMEDIATE-MASS STARS

To understand the global scenario of star formation around NGC 7419, we use NIR JHK_s data for point sources within a square degree region centred on $R.A._{J2000} = 22^h 52^m 28^s$ and

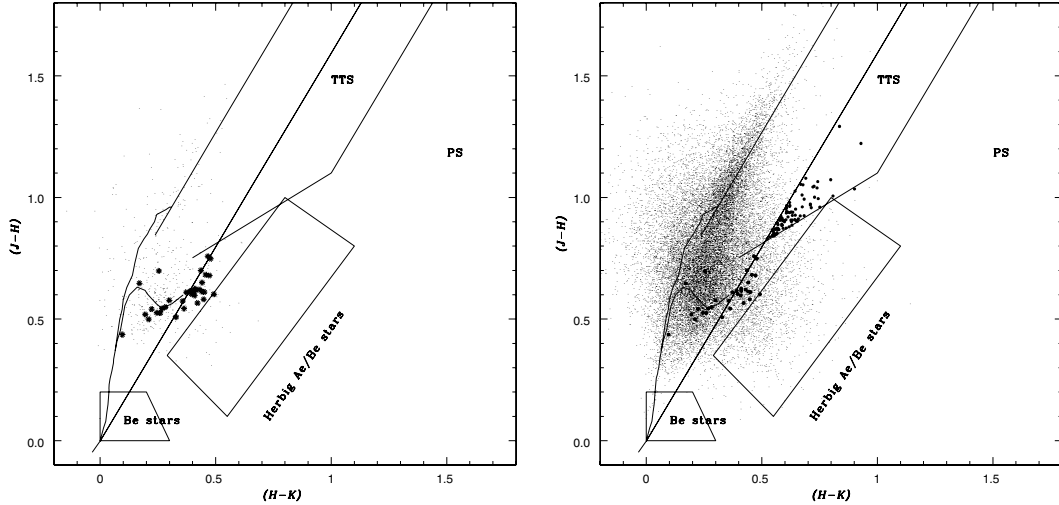


Figure 8. Colour–colour diagrams using the 2MASS JHK data. Left-hand panel: the NIR colour–colour diagram for the cluster region NGC 7419. Small dots represent the NIR stars present in cluster region and the asterisks denote the $H\alpha$ emission-line stars from Table 6. Right-hand panel: same as the left-hand panel, but for the square degree surrounding region centred at $R.A._{J2000} = 22^{\text{h}}52^{\text{m}}28^{\text{s}}$ and $Dec._{J2000} = +60^{\circ}53'52''$. Bigger filled dots denote 90 TTS in this region.

$Dec._{J2000} = +60^{\circ}53'52''$, which is 14.23 arcmin west from the cluster centre. It contains the entire cluster and the surrounding star-forming region. Data have been obtained from the 2MASS Point Source Catalog (PSC; Cutri et al. 2003). We have selected the sources based on the ‘read flag’ which gives the uncertainties in the magnitudes. We retain 2MASS sources with ‘read flag’ values of 1–2 for good quality data in our analysis. The JHK_s colours were transformed from 2MASS system to California Institute of Technology system using the relations given on the 2MASS web site.⁴

4.1 Colour–colour diagrams

The $(J - H)$, $(H - K)$ colour–colour diagram is plotted for the cluster region (471 stars) and the surrounding square degree region (22 100 stars), in Fig. 8. Solid lines represent unreddened main sequence and giant branch (Bessell & Brett 1988). The parallel solid lines are the reddening vectors for early- and late-type stars (drawn from the base and the tip of two branches). Location of T Tauri stars (TTS; Meyer, Calvet & Hillenbrand 1997), protostar (PS) like objects, classical Be stars and Herbig Ae/Be (Dougherty et al. 1994; Hernandez et al. 2005) are also shown. The extinction ratio $A_J/A_V = 0.282$, $A_H/A_V = 0.180$ and $A_K/A_V = 0.116$ have been taken from Cardelli et al. (1989). Stars below the reddening vectors are considered to have NIR excess. The asterisks represent all the stars with $H\alpha$ emission (Table 6). Out of 44 emission-line stars only 39 stars have NIR counterparts within 3 arcsec. NIR excess is shown by 17 emission-line stars within the cluster region but four more emission-line stars are situated at the boundary of the reddening vector, therefore, they have also considered as NIR excess stars within error bars in colours. From spectroscopic studies, Subramaniam et al. (2006) have identified them as Herbig Ae/Be stars. Therefore, NGC 7419 is a peculiar cluster having such a large number of Herbig Ae/Be stars. In surrounding region, 90 sources are found in the T Tauri locus (Meyer et al. 1997). These sources are considered to be mostly classical TTS (class II objects) with large NIR excesses and belong to the YSO population. There may

be an overlap in NIR colours of Herbig Ae/Be stars and TTS in the TTS region (Hillenbrand et al. 1992). Such a large number of young stars represent the youth of this region. However, all the TTS with NIR excesses are situated outside the cluster region.

4.2 Cluster age from Herbig Ae/Be stars

Fig. 9 shows M_V , $(V - I)_0$ CMD for $H\alpha$ emission stars (open circles; Table 6), NIR excess stars (black dots), stars with X-ray counterpart (asterisks; Section 8.3). Star BMD 950 is not shown as it shows a large error (> 0.1 mag) in I band. It is seen that most of Herbig Ae/Be stars are located to the right-hand side of the

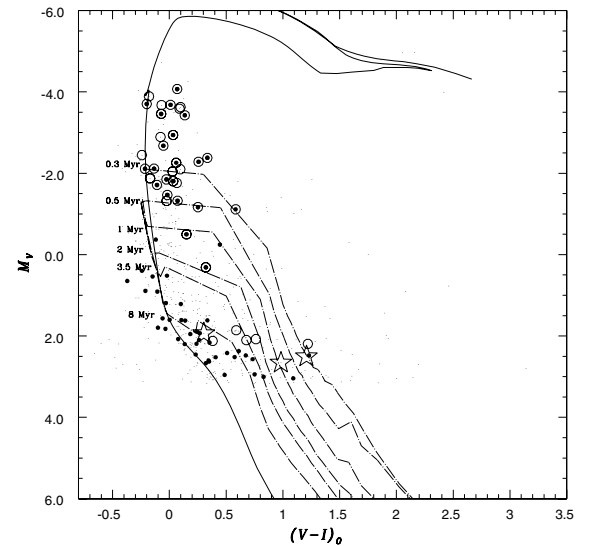


Figure 9. CMD M_V , $(V - I)_0$ of the cluster region. Open circles denote stars with $H\alpha$ emission (Table 6), asterisks denote stars with X-ray counterparts and having membership probability from X-ray colours while filled dots represent stars with NIR excess. Post-main-sequence isochrone for 25 Myr by GRD02 (continuous line) and pre-main-sequence isochrones for 0.3, 0.5, 1, 2, 3.5 and 8 Myr by SES00 (dashed lines) are also shown. Isochrones are corrected for a distance of 3.23 kpc.

⁴ <http://www.astro.caltech.edu/~jmc/2mass/v3/transformations/>

main sequence and to estimate their age, we use pre-main-sequence isochrones from Siess, Dufour & Forestini (2000, hereafter SES00) for ages 0.3, 0.5, 1, 2, 3.5 and 8 Myr, shown with dashed lines in Fig. 9. For reference, the post-main-sequence isochrone of 25 Myr age (GRD02) have been shown by continuous lines. Only one X-ray source and three emission-line stars lie in the range of 3.5–8 Myr isochrones, which may arise due to field star contamination of the Herbig Ae/Be stars loci in the NIR colour–colour diagram (Fig. 8). Therefore, considering only the large number of Herbig Ae/Be stars, i.e. emission-line stars with NIR excess, it is very likely that the turn-on age of the cluster cannot be more than 2 Myr.

4.3 Mass of Herbig Ae/Be stars using NIR colour–magnitude diagram

Stellar masses are determined using NIR colour–magnitude J , $(J - H)$ diagram. We prefer J over H or K , as the J waveband is less affected by the emission from circumstellar material (Bertot, Basri & Bouvier 1988). Left-hand panel of Fig. 10 shows NIR CMD for the cluster region NGC 7419. The 4-Myr post-main-sequence isochrone (GRD02) and pre-main-sequence evolutionary tracks for mass range $2-7 M_{\odot}$ (SES00) are plotted assuming a distance of 3.2 kpc and a mean reddening $E(B - V)$ of 1.70 mag (Sections 3.3 and 3.5). Reddening and extinction corrections to the isochrone and tracks are made using the relation $A_J/A_V = 0.282$ and $A_{(J-H)}/A_V = 0.102$ (Cardelli et al. 1989), where $A_V = 3.1E(B - V)$. Location of 21 Herbig Ae/Be stars in NIR CMD is represented by open circles and it is seen that 66 per cent of these are located between the mass range 5 and $7 M_{\odot}$. Only two stars lie in the mass range $3-4 M_{\odot}$.

Right-hand panel of Fig. 10 represents NIR CMD for 90 probable YSO candidates (shown with filled circles) identified in a square degree region around the cluster (Fig. 8). None of these YSOs is present in the cluster region and hence we argue that the population of YSOs is most likely associated with a local arm molecular cloud Sh2–154 (Ungerechts, Umbanhowar & Thaddeus 2000), see Section 5 for detailed discussion. We, therefore, correct the theoretical isochrones (SES00), for extinction assuming the cloud distance

of 1.4 kpc (Khalil, Joncas & Nekka 2004) and for reddening assuming a value of 0.4 mag kpc^{-1} towards the direction of NGC 7419 (Joshi 2005). The corrected isochrones are shown with solid curves in the right-hand panel of Fig. 10 and they trace the locus of 6-Myr pre-main-sequence stars having masses in the range $0.1-3 M_{\odot}$. It is observed that masses of all of the YSOs lie in the range $0.1-2.0 M_{\odot}$ indicating them to be TTS. Therefore, almost all of the YSO candidates are low-mass pre-main-sequence stars.

5 SPATIAL DISTRIBUTION OF LOW-MASS PRE-MAIN-SEQUENCE CANDIDATES

In Fig. 11, we show a square degree R -band image, reproduced from Digital Sky Survey (DSS),⁵ of the field containing YSO candidates and the cluster NGC 7419. Inner ($r \leq 1$ arcmin) and outer ($r \leq 3.5$ arcmin) boundaries of the cluster are encircled. Point sources from MSX which surveyed the Galactic plane in four mid-infrared bands – A (8.28 μm), C (12.13 μm), D (14.65 μm) and E (21.34 μm) at spatial resolution of ~ 18 arcsec (Price et al. 2001) – are also shown in Fig. 11. Information about 10 IRAS point sources and eight MSX point sources are given in Tables 9 and 10, respectively. The MSX sources are denoted by white open circles while asterisks represent IRAS sources. YSO candidates are denoted by open square boxes. Of eight MSX sources, six are identified with five supergiants and a carbon star and the other two are G108.6966+01.0686, a carbon star VMW Cep (Kukarkin et al. 1968), and G109.2152+01.6007, a semiregular pulsating star V386 Cep (Stephenson 1984). The cluster supergiants also have IRAS counterpart, and their presence in NGC 7419 is also supported from mid-infrared data.

In the following, we describe the attenuation properties of a square degree region around the cluster (see Section 4). Dobashi et al. (2005) recently produced extinction maps of the entire region of the Milky Way in the galactic latitude range $b \leq 40^\circ$ by applying traditional star count technique to the optical DSS sources. We retrieved the FITS images of the extinction map of the field containing NGC 7419 and their surrounding region from their on-line

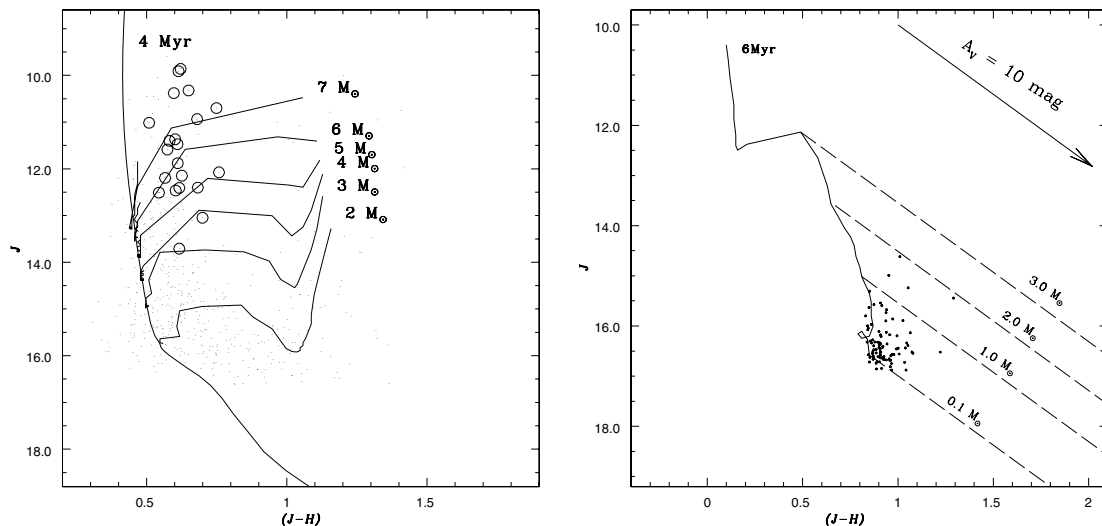


Figure 10. Stellar mass estimate using NIR CMD diagram. Left-hand panel: J , $(J - H)$ CMD for Herbig Ae/Be stars in the cluster region NGC 7419 are shown with open circles. The 4-Myr post-main-sequence isochrone (GRD02) and the pre-main-sequence evolutionary tracks for masses $2-7 M_{\odot}$ are also shown and indicated. Right-hand panel: same as left-hand panel but for the YSO candidates (asterisks) in the surrounding square degree region of NGC 7419. Solid curve denotes pre-main-sequence isochrone of 6-Myr (SES00), while the dashed oblique reddening lines denote the positions of pre-main-sequence stars for masses 0.1, 1, 2 and $3 M_{\odot}$.

⁵ DSS – <http://stduu.stsci.edu/dss/>

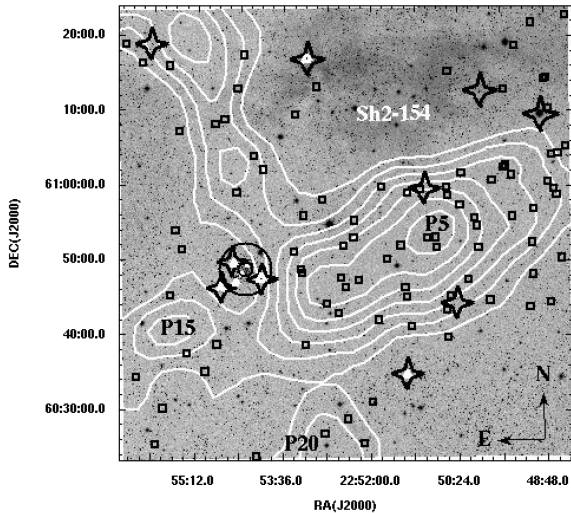


Figure 11. A square degree R -band DSS image of the field surrounding the cluster NGC 7419. North is up and east is to the left. Open boxes show the candidate YSOs, white thick dots represent MSX sources and open star symbols denote IRAS point sources. Inner ($r \leq 1$ arcmin) and outer boundaries ($r \leq 3.5$ arcmin) of NGC 7419 are encircled. The location of Sharpless nebula Sh2–154 is also marked. The dust extinction maps produced using star counting method are overlaid by white contours, and the associated clumps P5, P15 and P20 with cloud 699 are also marked (Dobashi et al. 2005).

website.⁶ In Fig. 11, we overlay the contours of high-resolution extinction map. The contours are plotted at $A_V = 2.5$ to 4.5 with an interval of 0.3 mag. The extinction towards the location of the cluster shows relatively low ($A_V \leq 2.5$) values, in comparison to the outer region of the cluster especially, towards the west, the east and the south, where extinction increases up to ~ 4.5 , ~ 3.2 and ~ 3.0 mag, respectively. These enhanced attenuations are identified with the dense cloud clumps P5, P15 and P20 of dark cloud 699 (Dobashi et al. 2005). Using star count method it would be difficult to detect dust obscuration located at a cluster distance of ~ 3.2 kpc, as the cloud would become inconspicuous due to large number of foreground stars (Dobashi et al. 2005; Medhi et al. 2008). We, therefore, argue that the dust obscuration would be due to a foreground cloud.

In order to see the dust emission characteristics of this cloud, we superimpose the IRAS 100- μm contours obtained from the Infrared Processing and Analysis Center (IPAC) on R -band DSS image in Fig. 12, left-hand panel. The IRAS survey was done in four bands 12, 25, 60 and 100 μm from mid-infrared to far-infrared. The contours are plotted after smoothing the IRAS 100- μm image. The contours are drawn at 134 (outermost) to 204 with the increment of 10 M Jy sr^{-1} . The IRAS dust emissions support the presence of dust obscuration at the location of cloud clumps P5, P15 and P20. The star count extinction map is seen to be highly correlated with the 100- μm IRAS dust map and represents the same morphology of the cloud. We also show the ^{12}CO temperature map of the region, see right-hand panel of Fig. 12 (Kerton & Brunt 2003). The contours are drawn for temperature ranges 6.5–9.5 K with the increment of 0.5 K. The peak of CO emission is most likely associated with clump P5 (~ 5.5 arcmin westward). A slight mismatch might be the effect of low resolution of the extinction map (Dobashi et al. 2005). It is

Table 9. IRAS point sources present in the square degree region centred about $R.A._{J2000} = 22^{\text{h}}53^{\text{m}}26^{\text{s}}$ and $\text{Dec}_{J2000} = +60^{\circ}53'52''$. ID 44 is a carbon star.

ID	IRAS PSC	F_{12} (Jy)	F_{25} (Jy)	F_{60} (Jy)	F_{100} (Jy)	Remark
–	22493+6018	7.04	2.39	3.12	48.91	VMW Cep
42	22527+6030	2.53	0.77	17.05	87.48	VMZ Cep
–	22525+6033	112.10	92.30	17.05	50.10	M7.5 Iab
14	22520+6031	3.10	1.06	17.05	50.87	M3.5 Iab
–	22512+6100	108.50	93.30	16.68	15.27	V386 Cep
–	22538+6102	1.04	0.49	6.50	70.00	–
–	22486+6028	0.85	0.37	4.95	53.07	–
–	22490+6043	0.54	0.35	5.35	39.51	–
–	22469+6053	0.46	0.25	5.55	71.76	–
–	22480+6056	0.30	0.25	5.34	68.93	–

Table 10. Same as for Table 9 except for the MSX point sources.

ID	Name MSX PSC	F_A (Jy)	F_B (Jy)	F_C (Jy)	Remark
–	G108.6966+01.0686	6.70	5.80	3.72	VMW Cep
–	G109.1599+01.1206	87.83	133.58	96.95	M7.5 Iab
42	G109.1632+01.0645	3.31	2.14	1.48	VMZ Cep
5	G109.1353+01.1118	3.40	2.00	1.68	M2.5 Iab
4	G109.1302+01.1321	3.43	2.11	1.33	M2.5 Iab
7	G109.1445+01.0947	1.71	0.71	0.74	M2.5 Iab
14	G109.0901+01.1184	3.38	2.41	1.58	M3.5 Iab
–	G109.2152+01.6007	63.48	83.70	66.06	V386 Cep

seen that 60 per cent of total YSO population seems to be associated with the clumpy region P5. Therefore, the clump P5 may provide a fertile environment for the formation of the low-mass stars.

Interestingly, the spatial distribution of TT stars is highly correlated with the extinction and IRAS dust map (see Figs 11 and 12), it is therefore likely that the population of YSOs (Section 4) might be associated with the foreground dark cloud. Avedisova (2002) identify a local arm star-forming region Sh2–154, situated in the north-east direction from the cluster. Optical diameter and distance of Sh2–154 are estimated, respectively, as 60 arcmin and 1.4 kpc (Blitz, Fich & Stark 1982). Hence, the YSO population (Fig. 8) could be part of Sh2–154 and associated with a dark cloud clump 699/P5 or 699/P15 as identified by Dobashi et al. (2005).

The effect of environment on the production of the low-mass stars has been investigated with the help of the distribution of the reddening in the cloud by assuming that they are situated at the same distance. The A_V value for each star was measured by tracing back to the intrinsic lines along the reddening vector found in Meyer et al. (1997). The value of A_V is found to vary from 0 to 3 mag. Only one YSO has $A_V \sim 5$ mag. The spatial distribution of the A_V from 0 to 5 mag is shown in Fig. 13, left-hand panel. No spatial gradient of A_V is found with the spatial distribution of the YSOs. The frequency distribution of A_V (Fig. 13, right-hand panel) represents that 77 per cent YSOs are having A_V less than 1.0 mag and 15 per cent of YSOs with A_V in between 1.0 to 2.0 mag. It shows that the environment for the YSOs is almost similar.

The effect of the youthfulness of the YSOs in the spatial distribution can also be investigated with the help $(H - K)_{\text{excess}}$, which is expected due to the presence of the circumstellar disc dissipating with time (Oasa et al. 2006). For YSOs, it is determined by

⁶ <http://darkclouds.u-gakugei.ac.jp/astromer/astromer.html>

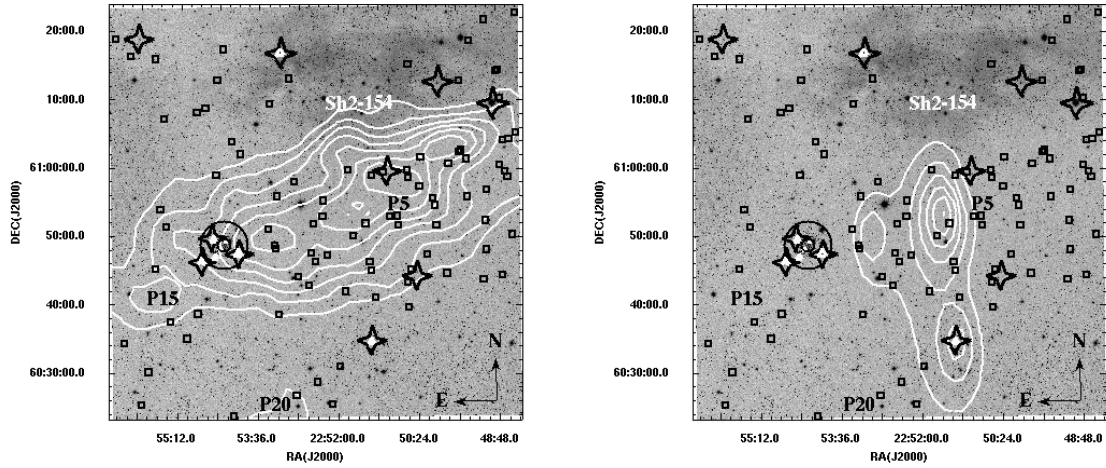


Figure 12. Same as Fig. 11 but white counters represent in left-hand panel: contours of 100- μm IRAS dust emissions, in right-hand panel: ^{12}CO temperature map (Kerton & Brunt 2003).

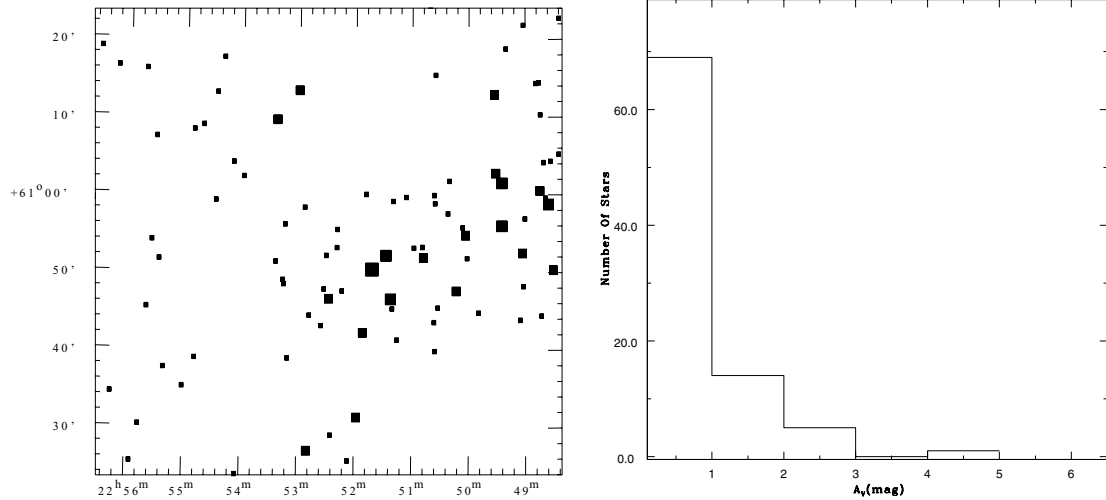


Figure 13. Distribution of the reddening. Left-hand panel: spatial distribution of the reddening of the YSO candidates. Increasing sizes of filled boxes represent YSOs having A_V with ranges 0–1, 1–2, 2–3 and 4–5 mag, respectively. x -axis and y -axis denote R.A._{J2000} and Dec._{J2000} , respectively. Right-hand panel: frequency distribution of the reddening for YSO candidates.

the method used in Matsuyanagi (2006) and it lies in the range 0.002–0.3 mag. The distribution of $(H - K)_{\text{excess}}$ (Fig. 14, left-hand panel) does not show any spatial gradient with distribution of the YSOs, indicating that the YSOs having different age are distributed uniformly within the cloud. Frequency distribution of the $(H - K)_{\text{excess}}$ is shown in Fig. 14, right-hand panel, and it indicates that 89 per cent of YSOs have nearly similar age. This represents a uniform distribution of the star formation rate within the cloud.

The morphology of the cloud is almost the same for all the YSOs and we find very little age dispersion in the YSOs. There is no significant contribution of the external agents found in the formation of these YSOs in this cloud. Therefore, such a uniform distribution of YSO candidates might be the result of primordial fragmentation.

6 MASS FUNCTION

The initial mass function (IMF) is the distribution of stellar masses that form in a star formation event in a given volume of space. It

is an important result of star formation and together with the star formation rate, the IMF dictates the evolution and fate of galaxies and star clusters (Kroupa 2002). However, the direct determination of IMF is not possible due to the dynamical evolution of stellar systems. Therefore, we derived MF which is often expressed by the power law, $N(\log m) \propto m^\Gamma$ and the slope of the MF is given as

$$\Gamma = d \log N(\log m) / d \log m, \quad (2)$$

where $N(\log m)$ is the number of star per unit logarithmic mass interval. In the solar neighbourhood the classical value derived by Salpeter (1955) is $\Gamma = -1.35$. In order to estimate the MF for the cluster region, we have used statistically cleaned sample described in Section 3.2. We have divided statistically cleaned sample for two star formation episodes. The first star formation episode is at 25 Myr and the masses corresponding to $V \leq 21$ mag have reached to the main sequence, therefore, only main-sequence MF have been considered for this episode. In Fig. 15, the MS represents the main-sequence band (selected in Section 3.2) and is drawn by

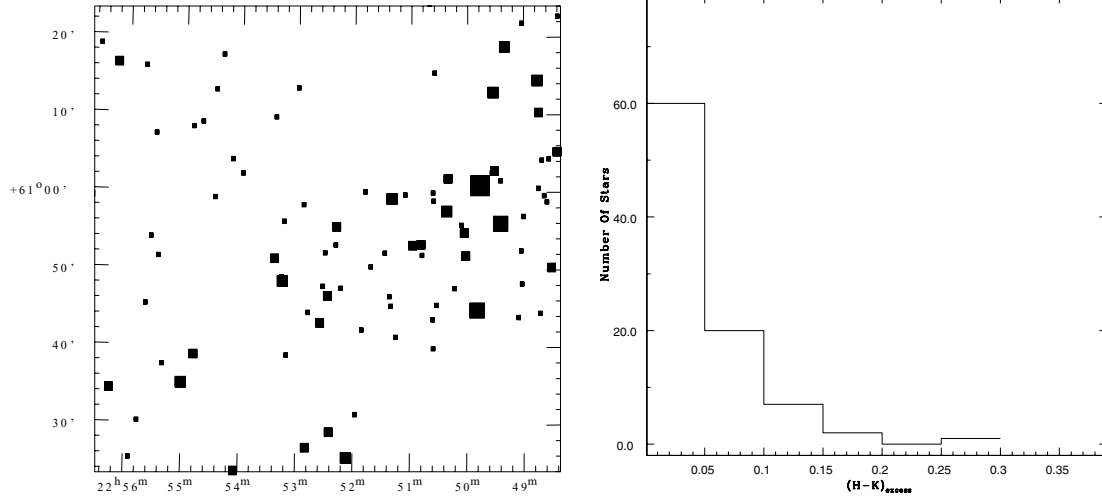


Figure 14. Age spread of YSOs. Left-hand panel: spatial distribution of the $(H - K)_{\text{excess}}$ of the YSO candidates. The increasing sizes of filled boxes represent the YSOs having $(H - K)_{\text{excess}}$ in ranges 0–0.05, 0.05–0.10, 0.10–0.15, 0.15–0.20 and 0.25–0.30 mag, respectively. x -axis and y -axis denote R.A._{J2000} and Dec._{J2000}, respectively. Right-hand panel: frequency distribution of the $(H - K)_{\text{excess}}$ for YSO candidates.

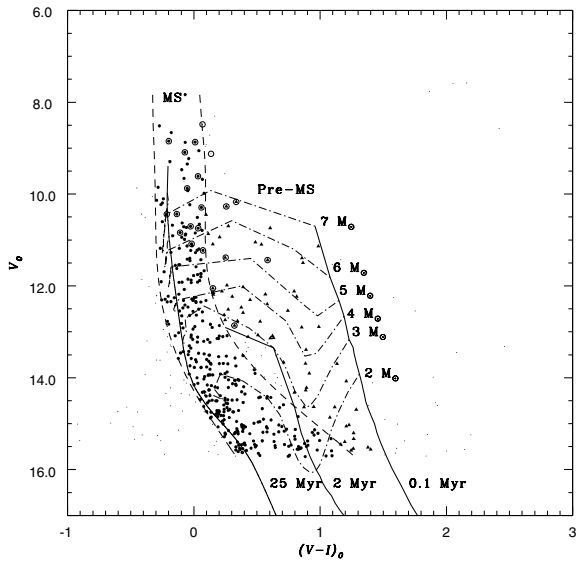


Figure 15. Extinction-corrected CMD at mean $E(B - V) = 1.70$ mag. Solid lines represent the theoretical isochrones for main sequence at 25 Myr (GRD02) and pre-main-sequence at 2 and 0.1 Myr (SES00). Solid dots within long-dash line show the stars selected for the estimation of main-sequence MF at 25 Myr, i.e. first episode of star formation, while the triangles represent the stars used for pre-main-sequence MF. Herbig Ae/Be are shown by open circles. Herbig Ae/Be stars within main-sequence band (solid dots with open circles) have not been considered in estimation of main-sequence MF and included in the estimation of pre-main-sequence MF.

long-dashed lines. The stars within this band are shown by solid dots. The main-sequence theoretical isochrone from GRD02 is shown by solid line at 25-Myr age with upper limit at $V \approx 15.0$ mag because the stars above this point have been evolved from the main sequence. Because of the above-mentioned reasons, we have considered the stars with V magnitude ranges 15–21 mag for the main-sequence MF. The second episode is at age ≤ 2 Myr, therefore, pre-main-sequence MF has been derived for the stellar population attached with this episode. The pre-main-sequence theoretical

isochrones by SES00 have been drawn by solid lines for ages 2 and 0.1 Myr (upper limit of age in model), and by dashed lines with dots for masses ranges from 2 to 7 M_{\odot} , respectively. The stars which are lying in between this age range have been used for the estimate of pre-main-sequence MF and shown by triangles in Fig. 15. The Herbig Ae/Be stars, described in Section 4, are shown by open circles. All these stars are excluded in the estimation of main-sequence MF even though they are lying inside the selected MS band, and considered as pre-main-sequence stars and included in the estimation of pre-main-sequence MF. We have used the stars shown by triangles in Fig. 15 and the Herbig Ae/Be stars inside the MS band for the estimation of pre-main-sequence MF for masses down to $\sim 3 M_{\odot}$ due to the incompleteness of mass below this limit.

We have derived the MF from LF using the theoretical evolutionary models. The MF in two subregions, i.e. the inner ($r \leq 1$ arcmin) and the outer ($1 \leq r \leq 3.5$ arcmin) region of the cluster, respectively, as well as for the whole cluster region ($r \leq 3.5$ arcmin) are given in Table 11 and plotted in Fig. 16.

The slope of the MF of the main-sequence stars in the inner region of the cluster is estimated as $\Gamma = -0.19 \pm 0.15$, which is flatter than the Salpeter (1955) value, while for the stars in the outer region, $\Gamma = -1.52 \pm 0.18$, which is similar to the Salpeter (1955) value. The Γ value for the stars is thus steeper in the outer region indicating a preferential distribution of relatively massive stars towards the cluster centre indicating a segregation of stellar masses. The slope for the MF for the whole cluster is $\Gamma = -1.10 \pm 0.19$, which is similar to the Salpeter value in the mass range of 8.6–1.4 M_{\odot} . This value of the MF is similar to the value estimated by Beauchamp et al. (1994), i.e. $\Gamma = -1.25 \pm 0.10$ estimated at age ~ 14 Myr and distance ~ 2.3 kpc for the cluster region.

The slopes of the pre-main-sequence MF for the intermediate mass range 7–3 M_{\odot} in the cluster are derived as $\Gamma = +1.54 \pm 0.52$ for inner, $\Gamma = +1.64 \pm 1.52$ for outer and $\Gamma = +1.68 \pm 0.84$ for whole cluster region. The value of the pre-main-sequence MF slope is significantly flatter than the Salpeter value.

7 MASS SEGREGATION

There is evidence for mass segregation in a few Galactic as well as Large Magellanic Cloud (LMC) star clusters, with the highest

Table 11. The MF of the cluster NGC 7419. MS represent the MF for main-sequence population while PMS represents the MF for pre-main-sequence population. The numbers of probable cluster members (N) have been obtained after subtracting the expected contribution of field stars in Section 3.2. $\log \phi$ represents $\log N(\log m)$.

Magnitude range (V mag)	Mass range (M_{\odot})	Mean $\log(M_{\odot})$	Inner region N	Inner region $\log \phi$	Outer region N	Outer region $\log \phi$	Whole region N	Whole region $\log \phi$
MS								
15.0–16.0	8.59–7.10	0.894	9	2.036	6	1.860	15	2.258
16.0–17.0	7.10–5.20	0.789	11	1.912	16	2.075	27	2.302
17.0–18.0	5.20–3.57	0.642	14	1.933	27	2.218	41	2.400
18.0–19.0	3.57–2.45	0.479	16	1.991	34	2.318	50	2.486
19.0–20.0	2.45–1.78	0.326	13	1.972	65	2.671	78	2.750
20.0–21.0	1.78–1.44	0.207	14	2.172	96	3.008	110	3.067
PMS								
	7.00–6.00	0.544	4	1.505	7	1.748	11	1.945
	6.00–5.00	0.653	3	1.491	11	2.055	14	2.160
	5.00–4.00	0.740	5	1.800	4	1.703	9	2.056
	4.00–3.00	0.067	5	1.873	16	2.378	21	2.496

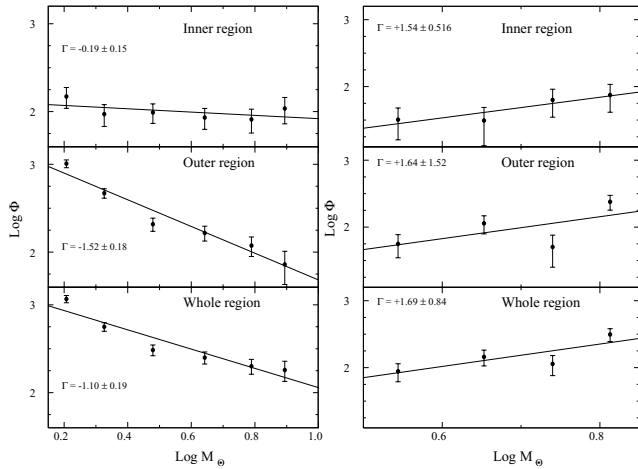


Figure 16. MF determination of MF in the various subregions of the cluster NGC 7419. Left-hand panel: for main sequence and for pre-main-sequence. Right-hand panel: inner region represents the core region ($r \leq 1$ arcmin), outer region represents the corona region ($1.0 \leq r \leq 3.5$ arcmin) and whole region represents the cluster region ($r \leq 3.5$ arcmin), as defined using radial density profile. The error bars represent $1/\sqrt{N}$ errors.

mass stars preferentially found towards the centre of the cluster (see Sagar et al. 1988; Sagar & Richtler 1991; Sagar & Griffiths 1998; Pandey et al. 2001, 2005; Kumar, Sagar & Melnick 2008). It is a well-accepted finding that stars in the clusters evolve rapidly towards a state of energy equipartition through stellar encounters, i.e. mass segregation. However, observations of very young clusters (e.g. Sagar et al. 1988; Pandey, Mahra & Sagar 1992; Hillenbrand 1997; Pandey et al. 2005) suggest that the mass segregation may be the imprint of star formation itself.

We have subdivided the main-sequence sample (used for the main-sequence MF in Section 6) into two mass groups ($3.6 \leq M/M_{\odot} < 8.6$; $1.4 \leq M/M_{\odot} < 3.6$) to characterize the degree of mass segregation in NGC 7419. Fig. 17 shows cumulative distribution of main-sequence stars as a function of radius in two different mass groups. Effect of mass segregation can be seen in this figure in the sense that more massive stars ($3.6 \leq M/M_{\odot} < 8.6$) tend to lie towards the cluster centre. The Kolmogorov–Smirnov (KS) test

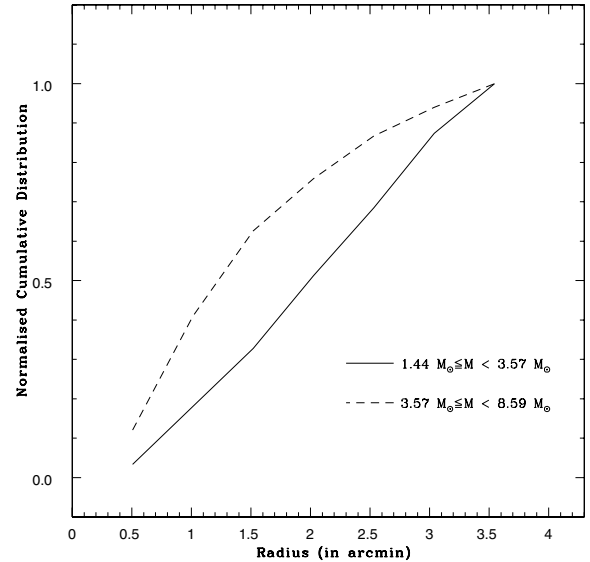


Figure 17. Cumulative radial distribution of main-sequence stars in mass intervals $1.44 \leq M/M_{\odot} < 3.57$ and $3.57 \leq M/M_{\odot} < 8.59$.

confirms the statement that the cumulative distribution of massive stars in the cluster is different from that of relatively less massive stars at a confidence level of 99 per cent. There is a strong evidence of mass segregation in the main-sequence stars within this cluster. We estimated the relaxation time to decide whether the mass segregation discussed above is primordial or due to dynamical relaxation. To estimate the dynamical relaxation time T_E , we have used the relation

$$T_E = \frac{8.9 \times 10^5 N^{1/2} R_h^{3/2}}{\bar{m}^{1/2} \log(0.4N)}, \quad (3)$$

where N is the number of cluster stars, R_h is the radius containing half of the cluster mass and \bar{m} is the average mass of the cluster stars (Spitzer & Hart 1971). The total number of stars in the cluster region is estimated as 321 in the mass range ($1.4 \leq M/M_{\odot} < 8.6$). For the half-mass radius, we have used half of the cluster extent, i.e. 1.63 pc. Taking average mass of the cluster as $3.92 M_{\odot}$, we have estimated the dynamical relaxation time T_E for the cluster as

Table 12. *XMM-Newton* observations of NGC 7419.

Parameter	NGC 7419
Observation ID	0201160501
Start time (UT)	2004 February 2 02:40:39
Stop time (UT)	2004 February 2 14:19:16
Usable time (ks)	39.62(MOS1), 40.21(MOS2), 35.35(PN)
EPIC mode	Full frame
Optical filter	Medium

8.0 Myr, which is lower than the turn-off age of the cluster, i.e. 19–25 Myr. Therefore, we can conclude that the cluster is dynamically relaxed.

8 X-RAY DATA ANALYSIS

We have used the archival X-ray data from the *XMM-Newton* observations of NGC 7419. The observations were proposed by Christian Motch to search for Be+white dwarfs binaries in NGC 7419. The observation details are given in Table 12. Our analysis is based on the CCD images from the European Photon Imaging Camera (EPIC). The details of the X-Ray Telescope and EPIC PN and MOS cameras are given by Jansen et al. (2001), Strüder et al. (2001) and Turner et al. (2001). Data reduction followed standard procedures using the *XMM-Newton* Science Analysis System software (SAS, version 7.0.0). Event files for MOS and PN are generated by using tasks EMCHAIN and EPCHAIN, respectively. Data from the three cameras were individually screened for high background episodes and the time intervals during which the total count rate (for single events of energy above 10 keV) in the instruments exceeded 0.35 and 1.0 count s⁻¹ for the MOS and PN detectors, respectively, were excluded.

8.1 Source detection and identification

The source detection is based on the SAS point source detection algorithm EDETECT_CHAIN. Three energy ranges were selected – a soft (S_X) band (0.3–0.7 keV), a medium (M_X) band (0.7–1.2 keV) and a hard (H_X) band (1.2–7.5 keV), and we built the corresponding images for the different instruments of the EPIC. Finally, source detection was performed on these images using EDETECT_CHAIN task, which is a chain script of various subtasks.

We inspected each source manually to reject false detections due to the instrumental artefacts, from the final list created by EMLDETECT task. In this way, we found 66 sources with a combined maximum likelihood value greater than 10 in all three instruments. The details of all the genuine X-ray sources in the energy band 0.3–7.5 keV are tabulated in Table 13 and shown in Fig. 18.

We cross-correlated the X-ray source list with our optical *UBVRI* photometric source list and NIR 2MASS All Sky data release data (Cutri et al. 2003) within the search radius 6 arcsec. The position of the stars in optical CCD is converted into R.A._{J2000} and Dec._{J2000} using the Guide Star Catalogue II (GSC 2.2, 2001). There are 18 X-ray sources with optical counterparts and 31 with NIR counterparts found after cross-correlation. Furthermore, none of the Herbig Ae/Be stars is having an X-ray counterpart. The unidentified X-ray sources, i.e. without having any optical or NIR counterparts within *XMM-Newton* field of view (FOV; 30 × 30 arcmin²), are 31 in number (47 per cent of the total).

8.2 The detection limit

The analysis of detection limits in the *XMM-Newton* FOV is equally important to decide the X-ray emission level of undetected Herbig Ae/Be stars, as none of the Herbig Ae/Be stars is emitting X-rays. The faintest source detected above 2σ in the *XMM-Newton* FOV has a count rate of 8.4×10^{-4} count s⁻¹ in the PN detector. The detection limit is not constant throughout the FOV because of the following three reasons: (a) a gap between the CCDs, and unoverlapped detector areas leading to a non-uniform effective detection area, (b) the decreasing exposure duration from the FOV centre to its edges, causing a non-uniformity in the effective exposure times as well and (c) the dense population of the stars near the centre of the cluster affecting the detection limit non-uniformly. We have neglected the effects of the gap between CCDs, as an approximation, and investigated the effects of other parameters on the detection limit.

We analysed the exposure map created by the EXPMAP task for the PN detector in the energy band 0.3–7.5 keV to derive the effect of exposure duration. It displays a smooth decrease in the counts from the centre of the FOV to its edges by about a factor of 3. If we are not considering the background effect, the signal-to-noise ratio is smaller by a factor of $\sqrt{3} \approx 1.7$ for the source at the edges of the FOV compare to the source at the centre. Therefore, the detection limit in the edges of the FOV will be twice the detection limit at the centre of the FOV due to the non-uniformity of exposure duration.

The variations in the detection limit due to the dense clustering at the centre of FOV have been determined using the approach by Sana et al. (2006). We computed an equivalent PN count rate in the energy band 0.3–7.5 keV due to the gap between CCDs. An empirical relation between count rates in the PN and MOS detectors was calculated and found to be approximately linear. For the sources which fall in the gaps between the PN CCDs, this relation is used to convert the MOS count rates into the PN count rates and these PN count rates are called pn-equivalent count rates. Fig. 19, left-hand panel, displays the source pn-equivalent count rates as a function of the distance from the centre of the FOV, i.e. the centre of the cluster NGC 7419. We adjusted a four-degree polynomial by selecting the faintest sources to derive an empirical detection limit in terms of pn-equivalent count rates (cr_{lim}) as a function of distance (d) from the centre of the FOV. This detection limit (in units of 10^{-3} count s⁻¹) is shown by a solid line in Fig. 19, left-hand panel, and described by the following relation

$$cr_{lim}(d) = 2.246 - 0.999d + 0.267d^2 - 0.028d^3 + 0.001d^4, \quad (4)$$

where the distance d is expressed in arcmin from the centre of the FOV. Left-hand panel of Fig. 19 shows that the detection limit is higher in centre of the FOV ($d < 3.5$ arcmin), which is the cluster region as decided in Section 3.1. It might be the effect of the extended X-ray emission from the cluster region, discovered in Section 8.5. The detection limit increases towards the CCD edges, as estimated by the exposure map. Using mission count rate simulator, WebPIMMS,⁷ we converted the pn-equivalent count rates into fluxes and luminosities. Assuming a hydrogen column density (N_H) of 9.9×10^{21} cm⁻², at $E(B - V) = 1.70$ mag for the cluster NGC 7419, the Raymond–Smith single temperature optically thin thermal plasma models were used at temperatures (kT) of 0.2, 1.0 and 2.0 keV. Results are displayed in Fig. 19, right-hand panel, for different plasma temperatures. Luminosities are calculated for the

⁷ WebPIMMS is a NASA’s HEASARC tool powered by PIMMS, version 3.9. It is hosted at URL: <http://heasarc.gsfc.nasa.gov/Tools/w3pimms.html>

Table 13. X-ray sources detected using `sas` task `edetect_chain`. Column 1 (XID) represents the identification number from X-ray source detection and display in Fig. 18, column 2 and column 3 (position) show source position from X-ray source detection, column 4 (count rates) represents the pn-equivalent count rates in energy band 0.3–7.5 keV, column 5 and column 6 (hardness ratio), HR1 and HR2, defined in text, the sign of \leq represents the hardness ratio calculated after replacing zero counts by upper limits in either of the energy band, column 7 (remarks) for PCM (the X-ray sources with membership probability using hardness ratio – the X-ray sources inside the dotted box in Fig. 20), IR (the X-ray sources with NIR counterparts within 6-arcsec search radius using 2MASS data), OPT (the X-ray sources with optical counterparts within 6-arcsec search radius using our *UBVR* photometry), CI (the X-ray sources within cluster region NGC 7419 – see Section 3.1).

XID	R.A. _{J2000} (h m s)	Dec. _{J2000} (° ′ ″)	Count rates (10 ⁻³ count s ⁻¹)	Hardness ratio		Remarks
				HR1	HR2	
1	22 52 35	60 47 37	10.92 ± 1.50	-0.40 ± 0.170	0.34 ± 0.21	IR
2	22 52 40	60 54 06	1.44 ± 0.58	0.25 ± 0.393	≤ -0.20	-
3	22 52 45	60 56 01	17.97 ± 1.58	0.16 ± 0.098	-0.19 ± 0.11	IR
4	22 52 46	60 54 00	2.61 ± 0.74	-0.01 ± 0.276	-0.58 ± 0.48	-
5	22 52 46	60 54 57	294.66 ± 5.33	0.47 ± 0.023	-0.37 ± 0.02	IR
6	22 52 49	60 50 01	3.89 ± 0.73	0.82 ± 0.357	0.28 ± 0.19	IR, PCM
7	22 53 05	60 39 19	4.83 ± 2.06	≤ -0.43	≤ 0.64	-
8	22 53 06	60 57 08	4.15 ± 0.83	0.19 ± 0.512	0.77 ± 0.26	-
9	22 53 17	60 38 13	2.82 ± 1.82	0.54 ± 0.565	≤ -0.63	IR
10	22 53 21	60 41 09	5.05 ± 0.73	0.21 ± 0.167	-0.10 ± 0.17	IR
11	22 53 22	60 58 08	2.20 ± 0.57	0.43 ± 0.255	≤ -0.43	-
12	22 53 23	60 46 12	3.91 ± 0.54	0.12 ± 0.145	-0.34 ± 0.18	IR
13	22 53 35	60 53 12	3.75 ± 0.59	0.71 ± 0.683	0.83 ± 0.21	PCM
14	22 53 36	60 55 47	3.38 ± 0.61	0.69 ± 0.421	0.54 ± 0.21	PCM
15	22 53 37	60 44 37	0.84 ± 0.31	≤ 0.64	0.67 ± 0.44	PCM
16	22 53 41	61 03 43	18.95 ± 2.03	0.40 ± 0.118	-0.50 ± 0.14	IR
17	22 53 42	60 59 38	3.18 ± 0.75	0.04 ± 0.233	-0.10 ± 0.31	IR
18	22 53 52	61 05 04	6.12 ± 1.14	≤ 0.97	0.71 ± 0.23	PCM
19	22 53 53	60 48 48	5.45 ± 0.55	0.83 ± 0.331	0.70 ± 0.12	IR, OPT, PCM, CI
20	22 53 57	60 59 14	1.32 ± 0.51	0.58 ± 0.406	-0.41 ± 0.46	IR
21	22 53 57	60 56 02	8.79 ± 0.96	≤ 0.85	0.88 ± 0.15	IR, PCM
22	22 54 00	60 54 15	1.56 ± 0.41	≤ 0.70	0.63 ± 0.31	PCM
23	22 54 00	60 48 22	2.56 ± 0.43	≤ 0.70	0.75 ± 0.21	OPT, PCM, CI
24	22 54 04	60 45 45	0.69 ± 0.24	0.08 ± 0.321	0.13 ± 0.19	IR, OPT
25	22 54 05	60 48 04	5.68 ± 0.71	0.07 ± 0.183	0.48 ± 0.16	IR, OPT, CI
26	22 54 07	60 43 54	1.75 ± 0.37	0.28 ± 0.230	-0.22 ± 0.26	IR, OPT
27	22 54 10	60 49 29	7.18 ± 1.17	-0.56 ± 0.352	0.84 ± 0.25	CI
28	22 54 11	60 55 23	5.96 ± 0.78	0.30 ± 0.137	-0.51 ± 0.18	IR
29	22 54 12	60 47 51	1.64 ± 0.37	≤ -0.48	0.75 ± 0.28	IR, OPT, CI
30	22 54 12	60 45 59	1.62 ± 0.33	0.09 ± 0.20	-0.98 ± 0.39	IR, OPT, CI
31	22 54 16	60 50 36	5.61 ± 0.73	-0.16 ± 0.17	0.41 ± 0.17	IR, OPT, CI
32	22 54 18	60 48 48	4.78 ± 0.71	≤ 0.37	0.53 ± 0.17	IR, OPT, CI
33	22 54 21	60 59 42	24.48 ± 1.52	0.02 ± 0.06	-0.65 ± 0.10	-
34	22 54 25	60 39 07	1.66 ± 0.40	0.49 ± 0.25	≤ -0.25	IR
35	22 54 27	60 48 44	1.40 ± 0.38	0.60 ± 0.52	0.50 ± 0.31	PCM, CI
36	22 54 29	60 43 49	1.64 ± 0.55	-0.06 ± 0.29	≤ -0.18	IR, OPT
37	22 54 29	60 35 57	7.26 ± 2.37	≤ -0.24	≤ 0.84	-
38	22 54 30	60 48 12	1.54 ± 0.36	0.85 ± 0.69	0.65 ± 0.28	OPT, PCM, CI
39	22 54 35	60 50 05	5.96 ± 1.05	0.60 ± 0.20	-0.43 ± 0.21	OPT, CI
40	22 54 39	60 41 03	4.48 ± 0.59	0.32 ± 0.14	-0.58 ± 0.19	IR
41	22 54 42	60 44 38	3.33 ± 0.84	≤ -0.14	≤ 0.79	IR, OPT
42	22 54 44	60 44 01	1.50 ± 0.39	≤ 0.46	≤ 0.60	-
43	22 54 46	60 48 27	1.09 ± 0.32	0.37 ± 0.91	0.80 ± 0.38	-
44	22 54 47	60 45 18	1.25 ± 0.34	≤ 0.78	≤ 0.56	PCM
45	22 54 49	60 52 01	1.14 ± 0.35	≤ 0.78	≤ 0.53	PCM
46	22 54 50	60 43 29	3.78 ± 0.54	0.93 ± 0.83	0.87 ± 0.19	OPT, PCM
47	22 54 55	60 47 42	2.25 ± 0.42	0.31 ± 0.21	-0.03 ± 0.22	IR, OPT
48	22 54 56	60 45 37	1.22 ± 0.36	0.43 ± 0.40	0.23 ± 0.32	IR, OPT
49	22 54 58	60 55 27	2.91 ± 0.56	≤ 0.74	0.88 ± 0.29	PCM
50	22 55 02	60 53 11	1.40 ± 0.48	≤ 0.86	≤ 0.60	PCM
51	22 55 05	60 36 45	4.92 ± 2.32	≤ 0.93	≤ 0.79	PCM
52	22 55 16	60 54 07	3.07 ± 0.60	0.97 ± 0.72	0.72 ± 0.24	IR, OPT, PCM
53	22 55 17	60 46 39	0.92 ± 0.37	≤ 0.70	0.82 ± 0.52	IR, OPT, PCM
54	22 55 22	60 53 52	3.12 ± 0.61	≤ 0.96	0.63 ± 0.23	PCM
55	22 55 22	60 58 10	12.19 ± 1.22	0.01 ± 0.11	-0.30 ± 0.14	IR
56	22 55 24	60 47 02	3.35 ± 0.97	-0.23 ± 0.64	0.76 ± 0.39	-

Table 13 – *continued*

XID	R.A. _{J2000} (h m s)	Dec. _{J2000} (° ′ ″)	Count rates (10 ⁻³ count s ⁻¹)	Hardness ratio		Remarks
				HR1	HR2	
57	22 55 27	60 57 18	2.14 ± 0.61	0.20 ± 0.27	-0.70 ± 0.44	-
58	22 55 30	60 41 35	4.14 ± 1.05	-0.62 ± 0.41	0.74 ± 0.42	-
59	22 55 31	60 51 39	6.48 ± 1.25	-0.46 ± 0.45	0.84 ± 0.28	-
60	22 55 34	60 42 23	1.85 ± 0.55	≤0.99	≤0.54	PCM
61	22 55 38	60 50 42	4.95 ± 0.77	≤0.87	≤0.79	PCM
62	22 55 44	60 50 43	5.48 ± 1.08	-0.76 ± 0.44	0.91 ± 0.32	-
63	22 55 46	60 46 48	7.41 ± 0.48	≤0.93	≤-0.12	PCM
64	22 55 47	60 44 58	9.86 ± 1.08	0.58 ± 0.13	-0.42 ± 0.13	IR
65	22 55 54	60 47 14	2.22 ± 0.63	0.10 ± 1.50	0.94 ± 0.39	-
66	22 55 56	60 56 50	2.94 ± 0.83	-0.02 ± 0.30	0.14 ± 0.37	IR

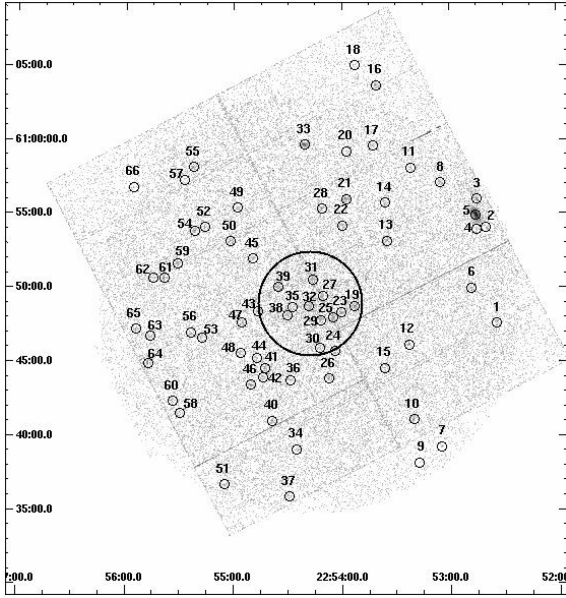


Figure 18. The X-ray point sources in the mosaic image of MOS and PN detector in the energy band 0.3–7.5 keV with their ID number as given in Table 13. x -axis and y -axis denote R.A._{J2000} and Dec._{J2000}, respectively.

distance of the cluster NGC 7419, i.e. 3.2 kpc. Within the cluster region ($d < 3.5$ arcmin), the detection limit of flux varies from 1.66×10^{-15} to 3.89×10^{-15} erg cm⁻² s⁻¹ for soft X-ray sources at $kT = 0.2$ keV, 3.02×10^{-15} to 6.31×10^{-15} erg cm⁻² s⁻¹ for X-ray sources at $kT = 1.0$ keV, and 4.47×10^{-15} to 10.0×10^{-15} erg cm⁻² s⁻¹ for X-ray sources at $kT = 2.0$ keV. We have estimated the detection limit of 21 Herbig Ae/Be stars, according to their positions in the cluster region using equation (4). As majority of Herbig Ae/Be stars have X-ray temperatures greater than 1.0 keV (Hamaguchi, Yamauchi & Koyama 2005; Stelzer et al. 2006), the detection limits for these stars are estimated as the median of the limiting X-ray luminosity (L_X) of Herbig Ae/Be stars, i.e. 5.20×10^{30} erg s⁻¹.

8.3 Probable members using hardness ratio

We have determined the X-ray hardness ratio HR1 and HR2 defined as

$$\text{HR1} = \frac{(M_X - S_X)}{(M_X + S_X)}, \quad (5)$$

$$\text{HR2} = \frac{(H_X - M_X)}{(H_X + M_X)}, \quad (6)$$

where S_X , M_X and H_X denote the soft band (0.3–0.7 keV), the medium band (0.7–1.2 keV) and the hard band (1.2–7.5 keV), respectively. For undetected sources, we used upper limits as a function of distance from the centre of FOV to its edges in each the energy bands using the method mentioned in Section 8.2. In cases where no counts are observed in any one energy band, the HR1 or HR2 are either +1.0 (no soft counts) or -1.0 (no hard counts), we have replaced the zero counts value by the upper limits depending upon the source position in the CCD in that energy band. The hardness ratios HR1 and HR2 of the X-ray sources in the *XMM-Newton* FOV are displayed in Fig. 20. X-ray sources are represented by solid dots, X-ray sources having optical counterparts, NIR counterparts and extended behaviour are denoted by open circles, open squares and the symbol of star, respectively. X-ray sources with rightward arrows represent the upper limits in HR1, and downward arrows represent the upper limits in HR2. Solid lines represent hardness ratios derived from model spectra.

We have simulated the values of HR1 and HR2 using plasma model APEC (Astrophysical Plasma Emission Code) to relate these hardness ratios to the spectral properties of the sources and to decide the membership of X-ray sources in the cluster region. Using the EPIC-pn response matrices within *XSPEC*, we have generated model spectra for monothermal plasma (1T-APEC) and two-temperature plasma (2T-APEC: the coronal X-ray emission from active late-type stars is generally not monothermal and consistent with the 2T thermal plasma models, see Tsujimoto et al. 2002; Favata et al. 2003; Stelzer et al. 2006). We considered plasma temperatures (kT) from 0.2 to 8.0 keV for 1T-APEC model, and kT1 from 0.2 to 0.8 keV with the combination of kT2 from 0.9 to 9.6 keV for 2T-APEC model at different hydrogen column density (N_H) = 1.0×10^{20} , 1.0×10^{21} , 4.9×10^{21} , 9.9×10^{21} (for cluster region), 19.8×10^{21} cm⁻².

The X-ray sources lying in between $1 \times 10^{20} < N_H < 1 \times 10^{21}$ cm⁻² are probably the foreground stars having either NIR counterparts or optical counterparts. As the value of mean N_H for the cluster is estimated as 9.9×10^{21} cm⁻² from the optical studies, X-ray stars located in between $4.9 \times 10^{21} < N_H < 19.6 \times 10^{21}$ cm⁻² belong to nearly the same cluster environment. In Fig. 20, the X-ray sources situated inside the dotted box are considered as probable members belonging to the cluster. Most of the X-ray sources inside this box are having only upper limits in the soft bands and have hard spectra, which is a consequence of the absorption of the soft components of the energy by the large column densities. A few sources are fitted neither by 1T-APEC model nor by 2T-APEC

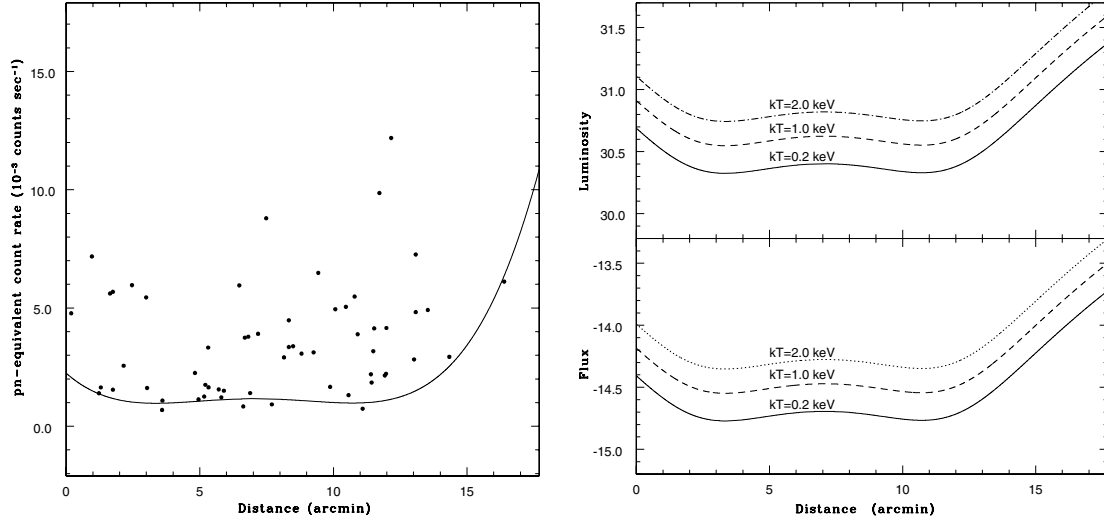


Figure 19. The variation of X-ray detection limits within *XMM-Newton* FOV in energy band 0.3–7.5 keV. Left-hand panel: the distribution of the pn-equivalent count rates of the X-ray sources as a function of their distance from the centre of the cluster NGC 7419. The solid line shows the adopted lower limit given in equation (4). (b) Right-hand panel: lower panel: estimated detection limit expressed in terms of the observed flux [$\log(\text{erg s}^{-1} \text{cm}^{-2})$], upper panel: the detection limit, expressed in luminosity [$\log(\text{erg s}^{-1})$] using the distance of the cluster NGC 7419.

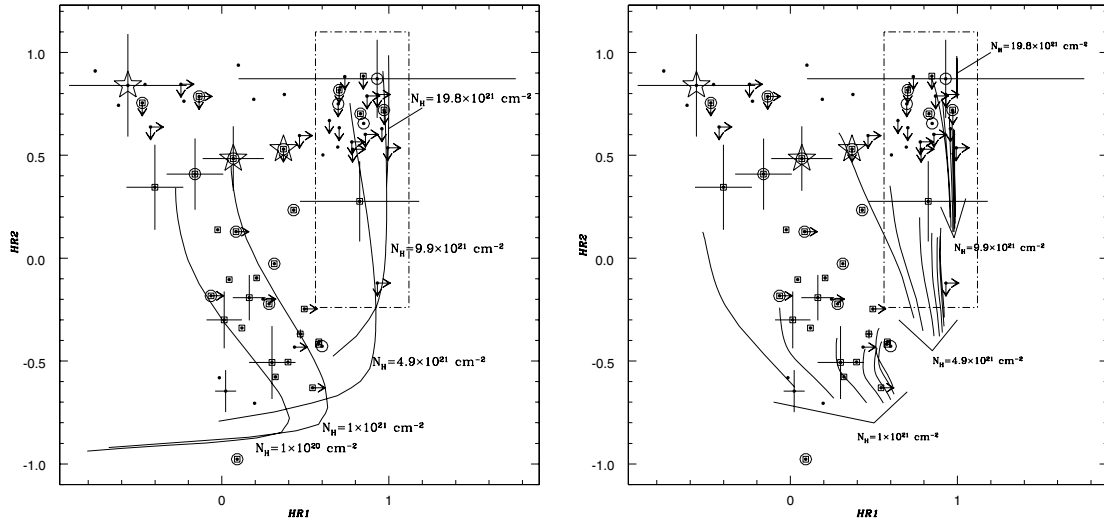


Figure 20. HR1 versus HR2 diagram for the X-ray sources denoted by solid dots. X-ray sources with optical counterparts, NIR counterparts and extended behaviour are denoted by open circles, open squares and the symbol of star, respectively. X-ray sources with rightward arrow represent the upper limits in HR1, and downward arrow represent the upper limits in HR2. Solid lines represent HR1 versus HR2 curves obtained from APEC model and dotted box contains the X-ray probable members sharing the cluster environment. Left-hand panel: for the single-temperature 1T-APEC plasma model, we considered plasma temperatures of kT ranges from 0.2 to 8.0 keV, at different hydrogen column density (N_H) = 1.0×10^{20} , 1.0×10^{21} , 4.9×10^{21} , 9.9×10^{21} (for cluster region), 19.8×10^{21} cm^{-2} . The temperature increases from bottom to top for each N_H value. Right-hand panel: the two-temperature 2T-APEC plasma model with $kT_1 = 0.2, 0.3, 0.4, 0.5, 0.6, 0.7, 0.8$ keV with the combination of kT_2 ranges from 0.9 to 9.6 keV, at different hydrogen column density (N_H) = 1.0×10^{20} , 4.9×10^{21} , 9.9×10^{21} (for cluster region), 19.8×10^{21} cm^{-2} . The temperature kT_1 increases from left to right for each N_H value with increasing kT_2 from bottom to top.

model and show a soft energy component as well as a hard energy component. Most of these sources are unidentified sources not having any NIR or optical counterparts. They may be the foreground stars, whose positions are uncertain in hardness ratio because of the large uncertainty in the hardness ratios. However, for a few X-ray sources, the uncertainty in hardness ratios is not so large that their location can be explained within the temperature range of the models. They may be either the foreground stars having very high hard energy component greater than 9 keV or the 1T-APEC and 2T-APEC model are not enough to characterize them.

8.4 X-ray luminosity function

X-ray luminosity function (XLF) is frequently employed to characterize a stellar population. We performed statistical analysis of XLF using Kaplan–Meier estimator of integral distribution functions. We have derived the median L_X of weak-lined and classical TTS in Taurus-Auriga region (age = 0.1–10 Myr) using the data from Stelzer & Neuhäuser (2001) and for Herbig Ae/Be stars, we have used the sample of Hamaguchi et al. (2005) and Stelzer et al. (2006). The median L_X of four probable members in the cluster is

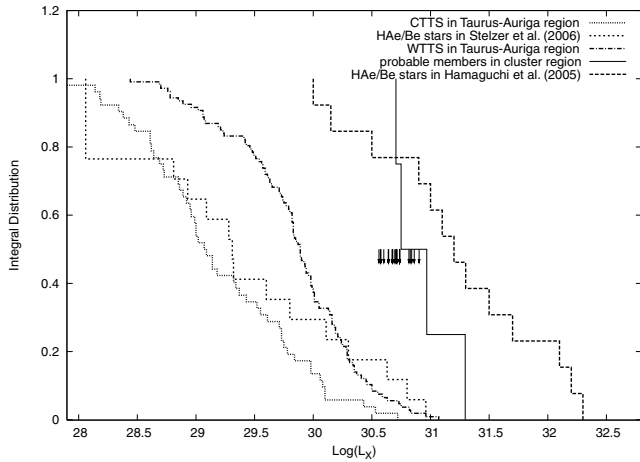


Figure 21. XLF for the probable members in the cluster region NGC 7419, weak-lined T Tauri stars (WTTS) and classical T Tauri stars (CTTS) in Taurus-Auriga region, and Herbig Ae/Be (H Ae/Be) stars from Stelzer et al. (2006) and Hamaguchi et al. (2005) using Kaplan–Meier estimator. The downward arrows represent 21 Herbig Ae/Be stars in the cluster NGC 7419.

estimated as 30.75 erg s^{-1} . For weak-lined TTS, classical TTS and Herbig Ae/Be stars in the sample of Hamaguchi et al. (2005) and Stelzer et al. (2006), the median L_X have been estimated as 29.88, 29.07, 29.29 and 31.15 erg s^{-1} , respectively. A comparison of the XLFs of TTS and Herbig Ae/Be stars with the cluster members are shown in Fig. 21.

The X-ray upper limits indicate that the Herbig Ae/Be stars in NGC 7419 are not systematically more active than TTS in Taurus-Auriga region and Herbig Ae/Be stars in Stelzer et al. (2006). However, the median value of XLF of Herbig Ae/Be stars in Hamaguchi et al. (2005) is more than the upper limits in the cluster. Our exposure and resolution (see Section 8.5) are not enough to reach the median value of L_X of TTS, therefore, we can not conclude whether Herbig Ae/Be stars can have an XLF similar to either the TTS or Herbig Ae/Be stars in Stelzer et al. (2006). A much deeper detection level is clearly needed in order to reach definitive conclusions concerning in the X-ray emission from Herbig Ae/Be stars. However, the more important conclusion to draw from this analysis is that the Herbig Ae/Be stars in NGC 7419 are not as active as in the sample of Hamaguchi et al. (2005).

8.5 Extended X-ray emission

The extended emission from the cluster region NGC 7419 has been studied using MOS images. PN data were not used since chip gaps, bad columns and the out-of-time event correction would have complicated the analysis. We have created the MOS images and associated exposure maps in three bands: soft band (0.3–0.7 keV), medium band (0.7–1.2 keV) and hard band (1.2–7.5 keV). We have chosen adaptive smooth style with signal-to-noise ratio 10 in the task `ASMOOTH`, for getting the faint emission from the cluster region. The resulting mosaic image with point sources are weighted, masked and exposure corrected following the procedure described in the documentation for the `SAS` task `ASMOOTH`.⁸ The point sources are removed from the image using cheese mask but the background is not subtracted from it.

⁸ <http://xmm.gsfc.nasa.gov/docs/xmm/sas/help/asmooth/index.html>

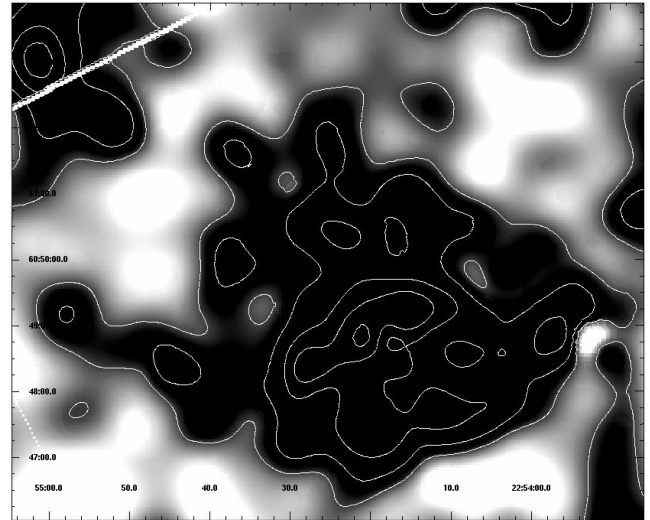


Figure 22. The X-ray extended emission from the cluster NGC 7419 in mosaic MOS detector in energy band 1.2–7.5 keV. x -axis and y -axis denote R.A._{J2000} and Dec._{J2000}, respectively. The grey-scale is logarithmic to highlight the diffuse component. The contours are plotted at 4.104 (above 3σ of the background), 4.644, 5.418, 6.192, $6.966 \times 10^{-3} \text{ count s}^{-1} \text{ arcmin}^{-2}$.

The signature of extended emission is not present in the soft band (0.3–0.7 keV) and medium band (0.7–1.2 keV) images of the MOS, because of the absorption of the soft X-ray component due to the large hydrogen column density (N_H). All the probable point sources have hard spectra, therefore, it is very likely that the extended emission is due to unresolved hard X-ray sources in the cluster. The X-ray contour map of the diffuse X-ray emission in energy band 1.2–7.5 keV is shown in Fig. 22. The entire cluster region is covered by the central CCD of the MOS, therefore, we have chosen background regions of 22 745 pixel beyond the diffuse emission but within the central CCD. The contours are plotted above the 3σ of the mean background count rates. The extended X-ray emission from the cluster region contains $0.084 \text{ count s}^{-1}$ in 14 611 pixel and corresponds to $5.76 \times 10^{-6} \text{ count s}^{-1} \text{ pixel}^{-1}$. The pixel size is set at $2 \times 2 \text{ arcsec}^2$. Therefore, the total extended emission has a size of 16.23 arcmin^2 . We have estimated the count rate from the extended emission as $1.38 \times 10^{-3} \text{ count s}^{-1} \text{ arcmin}^{-2}$, after subtracting the mean background count rate. Using `WebPIMMS`, ver3.9a, this count rate is converted into flux after considering Raymond–Smith thermal plasma model at 1 keV and estimated as $1.47 \times 10^{-14} \text{ erg s}^{-1} \text{ cm}^{-2} \text{ arcmin}^{-2}$, which corresponds to the luminosity $L_X \approx 1.8 \times 10^{31} \text{ erg s}^{-1} \text{ arcmin}^{-2}$ in the energy band 1.2–7.5 keV. We have chosen the beamwidth as 50 pixel, i.e. 5σ (smoothing beamwidth). We have estimated 18 beam elements in per arcmin^2 region and estimated L_X of unresolved sources as $1.0 \times 10^{30} \text{ erg s}^{-1}$. Therefore, we are expecting ~ 288 unresolved X-ray sources in the total diffuse component.

The L_X of unresolved X-ray sources is comparable with the L_X of TTS, i.e. $28 < \log L_X < 32$ in energy band 0.5–8.0 keV, with a peak around $\log L_X \sim 29$ (Feigelson et al. 2005). It can be explained by the presence of ~ 288 TTS in the cluster, which are not resolved by *XMM-Newton* Observatory. Higher resolution (subarcsec) data are urgently required to explore this issue.

8.6 X-ray emission and Herbig Ae/Be stars

We have examined a sample of 21 Herbig Ae/Be in this cluster using 2MASS data, $H\alpha$ photometry and the spectroscopic studies

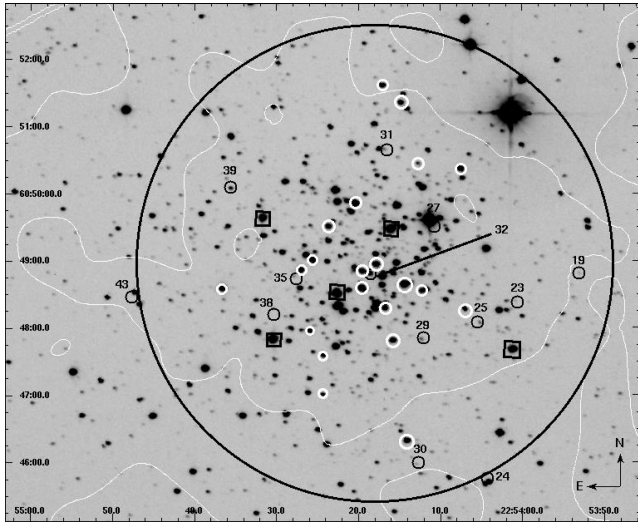


Figure 23. Overlay of X-ray point sources (black open circles) with ID from Table 13, and 21 Herbig Ae/Be stars (white open circles) in the cluster region NGC 7419. Large black circle represents the cluster region and black squares represent supergiants. x -axis and y -axis denote R.A._{J2000} and Dec._{J2000}, respectively. The white contours represent the extended X-ray emission in energy band 1.2–7.5 keV above the 3σ of the background count rate, i.e. the outermost contour of the Fig. 22.

reported by Subramaniam et al. (2006). However, none of Herbig Ae/Be stars has an X-ray counterpart. In Fig. 23, the distribution of the X-ray point sources which are having optical counterparts, supergiants (five in number) and the Herbig Ae/Be stars within the cluster are shown by black open circles (with ID from Table 13), black open squares and white open circles, respectively.

The detection limit analysis (Section 8.2) and the XLF (Fig. 21) indicate that the L_X observed from the low-mass pre-main-sequence stars is less than upper limits of the detection (see Stelzer & Neuhauser 2001), i.e. $28 < \log L_X < 32$ in energy band 0.5–8.0 keV, with a peak around $\log L_X \sim 29 \text{ erg s}^{-1}$ (Feigelson et al. 2005). Therefore, if a Herbig star is having a TTS as a binary companion, then we cannot detect the X-ray emission from it. Therefore, the generation of X-ray emission from Herbig Ae/Be stars (see Damiani et al. 1994; Zinnecker & Preibisch 1994; Stelzer et al. 2006) might be the result of a TTS binary companion which is not detectable in our study and we cannot rule out the companion hypothesis for the generation of X-ray emission from Herbig Ae/Be stars. It might happen that the Herbig Ae/Be star itself is emitting X-rays but the level of the X-ray emission is less than the detection limit. A similar kind of process as in TTS could then take place in the Herbig Ae/Be stars for the generation of X-rays.

9 SUMMARY AND CONCLUSIONS

A deep optical *UBVRI* and narrow-band $H\alpha$ observations along with multiwavelength archival data from the surveys such as 2MASS, MSX, IRAS and *XMM-Newton* are used to understand the global scenario of star formation and the basic parameters of the cluster NGC 7419. *XMM-Newton* archival data have also been used to study the X-ray emission mechanism from the cluster.

The radius of the cluster NGC 7419 has been found to be 4.0 ± 0.5 arcmin using radial density profile. The reddening law in the direction of the cluster is found to be normal at longer wavelengths but anomalous at shorter wavelengths. Reddening, $E(B - V)$, is found to be varying between 1.5 and 1.9 mag with a mean value

$\sim 1.7 \pm 0.2$ mag. The turn-off age and the distance of the cluster are estimated to be 22.5 ± 2.5 Myr and 3230^{+330}_{-430} pc, respectively. The MF for the main-sequence stars in the cluster is estimated as having $\Gamma = -1.10 \pm 0.19$ in the mass range $8.6 < M \leq 1.4 M_\odot$, which is a similar to the Salpeter (1955) value. Effect of mass segregation is found in the main-sequence stars which may be the result of dynamical evolution.

Using the NIR colour–colour diagram and narrow-band $H\alpha$ observations, we have identified 21 Herbig Ae/Be in the cluster region with the masses lying between 3 and $7 M_\odot$. The ages of these Herbig Ae/Be stars are found to be in the range of ~ 0.3 to 2.0 Myr. The significant difference between turn-off age and turn-on age of the cluster represents a second episode of star formation in the cluster. We have found 90 YSOs having masses in the range from 0.1 to $2.0 M_\odot$ with the help of NIR colour–colour diagram around the cluster. The presence of such a large number of NIR excess sources (TTS) shows a recent star formation episode in the surroundings of the cluster region. Using extinction, dust and ^{12}CO maps, we found that these YSOs are probably associated with a foreground star-forming region Sh-154 and not related with the cluster region. We found no obvious trend in spatial distribution of YSOs with A_V and $(H - K)_{\text{excess}}$. The dispersion in A_V and $(H - K)_{\text{excess}}$ is also very low which indicates that a majority of the YSOs are born at the same time in the same environment. Therefore, it is possible that primordial fragmentation of the cloud may be responsible for the formation of the low-mass stars within this cloud.

We have detected 66 X-ray sources in the observed field by *XMM-Newton* Observatory using archival X-ray data. Out of these sources, 23 are known to be the probable members of the cluster based on analysis of their X-ray colours. 15 X-ray sources are without any optical or NIR counterparts. These may be the young embedded sources which need to be investigated further. We have derived the detection limits of X-ray observations based on the position of the X-ray source in the FOV and on its energy spectrum. Thus, the median value for the detection limit for the 21 Herbig Ae/Be stars in the field is $L_X \sim 5.2 \times 10^{30} \text{ erg s}^{-1}$. We have compared the XLF for the cluster members with the TTS and Herbig Ae/Be stars. Because of insufficient exposure and resolution, the sensitivity was not enough to reach the level of the median X-ray luminosity observed in TTS in Taurus-Auriga region and Herbig Ae/Be stars in Stelzer et al. (2006). Therefore, a conclusive comparison of X-ray properties of the stars cannot be made. However, the comparison indicates that Herbig Ae/Be stars in NGC 7419 tend to be less X-ray luminous than in the sample of Hamaguchi et al. (2005), which shows that X-ray activity level of the Herbig Ae/Be stars is not more than in the TTS. Therefore, we can support the binary TTS companion hypothesis for the generation of X-rays in Herbig Ae/Be stars. It is also possible that a Herbig Ae/Be star is itself emitting X-rays but the level of the X-ray emission is similar to that of the TTS. The cluster region shows an extended X-ray emission with a total luminosity estimated to be $L_X \approx 1.8 \times 10^{31} \text{ erg s}^{-1} \text{ arcmin}^{-2}$. This diffuse emission might be the result of X-ray emission from TTS type which could not be resolved by *XMM-Newton* observations. It requires ~ 288 TTS each having $L_X \sim 1.0 \times 10^{30} \text{ erg s}^{-1}$, if it originates from such stars. High-resolution deep observations such as from *Chandra* are required for a detailed analysis of this cluster region.

ACKNOWLEDGMENTS

Authors are thankful to the anonymous referee for constructive comments. This publication makes use of data products from

XMM-Newton archives using the high energy astrophysics science archive research centre which is established at Goddard by NASA. We acknowledge Randall Smith from Goddard Space Flight Center NASA and *XMM-Newton* Help Desk for their remarkable support in X-ray data analysis. This research has also made use of data from the 2MASS, which is a joint project of the University of Massachusetts, the Infrared Processing and Analysis Center/California Institute of Technology, funded by the National Aeronautics and Space Administration and the National Science Foundation and VizieR catalogue access tool, CDS, Strasbourg, France. One of us (BK) acknowledges support from the Chilean Center of Astrophysics FONDAF No. 15010003.

REFERENCES

- Avedisova V. S., 2002, *Astron. Rep.*, 46, 193
 Barbon R., Hassan S. M., 1996, *A&AS*, 115, 325
 Baume G., Vázquez R., Carraro G., 2004, *MNRAS*, 355, 475
 Beauchamp A., Moffat A. F. J., Drissen L., 1994, *ApJS*, 93, 187
 Bertout C., Basri G., Bouvier J., 1988, *ApJ*, 330, 350
 Bessell M. S., 1979, *PASP*, 91, 589
 Bessell M. S., Brett J. M., 1988, *PASP*, 100, 1134
 Bhatt B. C., Pandey A. K., Mohan V., Mahara H. S., Paliwal D. C., 1993, *Bull. Astron. Soc. India*, 21, 33
 Blanco V., Nassau J. J., Stock J., Wehlau W., 1955, *ApJ*, 121, 637
 Blitz L., Fich M., Stark A. A., 1982, *ApJS*, 49, 183
 Caldwell J. A. R., Cousins A. W. J., Ahlers C. C., van Wamelen P., Maritz E. J., 1993, *South Afr. Astron. Obser. Circ.*, 15, 1
 Cardelli J. A., Clayton G. C., Mathis J. S., 1989, *ApJ*, 345, 245
 Caron G., Moffat A., St-Louis N., Wade G. A., 2003, *AJ*, 126, 1415
 Cutri R. M. et al., 2003, The IRSA 2MASS All-Sky Point Source Catalog. NASA/IPAC Infrared Science Archive (<http://irsa.ipac.caltech.edu/applications/Gator/>)
 Damiani F., Micela G., Sciortino S., Harnden F. R., Jr, 1994, *ApJ*, 436, 807
 Dias W. S., Alessi B. S., Moitinho A., Lépine J. R. D., 2002, *A&A*, 389, 871
 Dobashi K., Uehara H., Kandori R., Sakurai T., Kaiden M., Umemoto T., Sato F., 2005, *PASP*, 57, 1
 Dougherty S. M., Waters L. B. F. M., Burk G., Cote J., Cramer N., van Kerkwijk M. H., Taylor A. R., 1994, *A&A*, 290, 609
 Favata F., Giardino G., Sciortino S., Damiani F., 2003, *A&A*, 403, 187
 Feigelson E. D. et al., 2005, *ApJS*, 160, 379
 Fitzgerald M. P., 1970, *A&A*, 4, 234
 Girardi L., Bertelli G., Bressan A., Chiosi C., Groenewegen M. A. T., Marigo P., Salasnich B., Weiss A., 2002, *A&A*, 391, 195 (GRD02)
 Hamaguchi K., Yamauchi S., Koyama K., 2005, *ApJ*, 618, 360
 Hernandez J., Calvet N., Hartmann L., Briceno C., Sicilia-Aguilar A., Berlind P., 2005, *AJ*, 129, 856
 Hillenbrand L. A., 1997, *AJ*, 113, 1733
 Hillenbrand L. A., Strom S. E., Vrba F. J., Keene J., 1992, *ApJ*, 397, 613
 Huang F., Chen W. P., Hsiao W. S., 2006, *J. Taipei Astron. Mus.*, 4, 27
 Jansen F. et al., 2001, *A&A*, 365, 1
 Jeffries R. D., Oliveira J. M., Naylor T., Mayne N. J., Littlefair S. P., 2007, *MNRAS*, 376, 580
 Johnson H. L., 1968, in Middlehurst B. M., Aller L. H., eds, *Nebulae and Interstellar Matter*. Univ. Chicago Press, Chicago, p. 191
 Johnson H. L., Morgan W. W., 1953, *ApJ*, 117, 313
 Joshi Y. C., 2005, *MNRAS*, 362, 1259
 Kaluzny J., Udalski A., 1992, *Acta Astron.*, 42, 29
 Kerton C. R., Brunt C. M., 2003, *A&A*, 399, 1083
 Khalil A., Joncas G., Nekka F., 2004, *ApJ*, 601, 352
 King I., 1962, *AJ*, 67, 471
 Koornneef J., 1983, *A&A*, 128, 84
 Kroupa P., 2002, *Sci*, 295, 82
 Kukarkin B. V. et al., 1968, *Inf. Bull. Var. Stars*, 311, 1
 Kumar B., Sagar R., Sanwal B. B., Bessell M. S., 2004, *MNRAS*, 353, 991
 Kumar B., Sagar R., Melnick J., 2008, *MNRAS*, 386, 1380
 Landolt A. U., 1992, *AJ*, 104, 340
 Matsuyanaagi I., Itoh Y., Sugitani K., Oasa Y., Mukai T., Tamura M., 2006, *PASJ*, 58, 29
 Mayne N. J., Naylor T., Littlefair S. P., Saunders E. S., Jeffries R. D., 2007, *MNRAS*, 375, 1220
 Medhi B. J., Maheswar G., Pandey J. C., Kumar T. S., Sagar R., 2008, *MNRAS*, 388, 105
 Meyer M., Calvet N., Hillenbrand L. A., 1997, *AJ*, 114, 288
 Moffat A. F. J., Vogt N., 1973, *A&A*, 23, 317
 Naylor T., Jeffries R. D., 2006, *MNRAS*, 373, 1251
 Nilakshi N., Sagar R., 2002, *A&A*, 381, 65
 Oasa Y. et al., 2006, *AJ*, 131, 1608
 Pandey A. K., Mahra H. S., Sagar R., 1992, *Bull. Astron. Soc. India*, 20, 287
 Pandey A. K., Durgapal A. K., Bhatt B. C., Mohan V., Mahra H. S., 1997, *A&A*, 122, 111
 Pandey A. K., Nilakshi O. K., Sagar R., Tarusawa K., 2001, *A&A*, 374, 504
 Pandey A. K., Upadhyay K., Nakada Y., Ogura K., 2003, *A&A*, 397, 191
 Pandey A. K., Upadhyay K., Ougra K., Sagar R., Mohan V., Mito H., Bhatt H. C., Bhatt B. C., 2005, *MNRAS*, 358, 1290
 Phelps R. L., Janes K. A., Montgomery K. A., 1994, *AJ*, 107, 1079
 Pigulski A., Kopacki G., 2000, *A&A*, 146, 465
 Press W. H., Teukolsky S. A., Vetterling W. T., Flannery B. P., 1992, *Numerical Recipes in FORTRAN: The Art of Scientific Computing*. Cambridge Univ. Press, New York
 Price S. D., Egan M. P., Carey S. J., Mizuno D. R., Kuchar T. A., 2001, *AJ*, 121, 2819
 Sagar R., 1987, *MNRAS*, 228, 483
 Sagar R., Griffiths W. K., 1998, *MNRAS*, 299, 777
 Sagar R., Richtler T., 1991, *A&A*, 250, 324
 Sagar R., Miakutin V. I., Piskunov A. E., Dluzhnevskaja O. B., 1988, *MNRAS*, 234, 831
 Salpeter E. E., 1955, *ApJ*, 121, 161
 Sana H., Gosset E., Rauw G., Sung H., Vreux J.-M., 2006, *A&A*, 454, 1063
 Sandhu T. S., Pandey A. K., Sagar R., 2003, *A&A*, 408, 515
 Schmidt-Kaler Th., 1982, in Scaifers K., Voigt H. H., eds, *Landolt/Bornstein Group VI Vol. 2b, Numerical Data and Functional Relationship in Science and Technology*. Springer-Verlag, Berlin, p. 14
 Siess L., Dufour E., Forestini M., 2000, *A&A*, 358, 593 (SES00)
 Spitzer L., Jr, Hart M. H., 1971, *ApJ*, 164, 399
 Stelzer B., Neuhäuser R., 2001, *A&A*, 377, 538
 Stelzer B., Huéramo N., Micela G., Hubrig S., 2006, *A&A*, 452, 1001
 Stephenson C. B., 1984, *Publ. Warner Swasey Obser.*, 3, 1
 Stetson P. B., 1987, *PASP*, 99, 191
 Stetson P. B., 1992, in Worrall D. M., Biemesderfer C., Barnes J., eds, *ASP Conf. Ser. Vol. 25, Astronomical Data Analysis Software and Systems I*. Astron. Soc. Pac., San Francisco, p. 297
 Strüder L., Briel U., Dennerl K., Hartmann R., Kendziorra E., Meidinger N., Pfeffermann E., Reppin C., 2001, *A&A*, 365, 18
 Subramaniam A., Mathew B., Bhatt B. C., Ramya S., 2006, *MNRAS*, 370, 743
 Tsujimoto M., Koyama K., Tsuboi Y., Goto M., Kobayashi N., 2002, *ApJ*, 556, 574
 Turner M. J. L. et al., 2001, *A&A*, 365, 27
 Ungerechts H., Umbanhowar P., Thaddeus P., 2000, *ApJ*, 537, 221
 van de Hulst H. C., Mullar C. A., Oort J., 1954, *Bull. Astron. Inst. Neth.*, 12, 117
 Wegner W., 1994, *MNRAS*, 270, 229
 Whittet D. C. B., van Breda I. G., 1980, *MNRAS*, 192, 467
 Zinnecker H., Preibisch T., 1994, *A&A*, 292, 152

SUPPORTING INFORMATION

Additional Supporting Information may be found in the online version of this article:

Table 3. *UBVRI* and $H\alpha$ photometric data of the sample stars in 13×13 arcmin² region. *X* and *Y* positions of stars in the CCD are converted into $R.A._{J2000}$ and $Dec._{J2000}$ using the Guide Star Catalogue II (GSC 2.2, 2001).

Table 4. A comparison of present *UBVRI* CCD photometry with that present in the literature – viz Bhatt et al. (1993), Beauchamp et al. (1994) and Subramaniam et al. (2006).

Please note: Wiley-Blackwell are not responsible for the content or functionality of any supporting information supplied by the authors. Any queries (other than missing material) should be directed to the corresponding author for the article.

This paper has been typeset from a $\text{T}_{\text{E}}\text{X}/\text{L}_{\text{A}}\text{T}_{\text{E}}\text{X}$ file prepared by the author.